Dysfunction of the ciliary ARMC9/TOGARAM1 protein module causes Joubert syndrome

Brooke L. Latour,[1] Julie C. Van De Weghe,[2] Tamara D.S. Rusterholz,[3,4] Stef J.F. Letteboer,[1] Arianna Gomez,[2] Ranad Shaheen,[5] Matthias Gesemann,[4] Arezou Karamzade,[6] Mostafa Asadollahi,[6] Miguel Barroso-Gil,[7] Manali Chitre,[8] Megan E. Grout,[2] Jeroen van Reeuwijk,[1] Sylvia E.C. van Beersum,[1] Caitlin V. Miller,[2] Jennifer C. Dempsey,[2] Heba Morsy,[9] University of Washington Center for Mendelian Genomics,[10] Michael J. Bamshad,[2,10,11,12] Genomics England Research Consortium,[13] Deborah A. Nickerson,[10,11] Stephan C.F. Neuhauss,[4] Karsten Boldt,[14] Marius Ueffing,[14] Mohammad Keramatipour,[6] John A. Sayer,[7] Fowzan S. Alkuraya,[5,15] Ruxandra Bachmann-Gagescu,[3,4] Ronald Roepman,[1] and Dan Doherty[2,16]

[1]Department of Human Genetics and Radboud Institute for Molecular Life Sciences, Radboud University Medical Center, Nijmegen, Netherlands. [2]Department of Pediatrics, University of Washington, Seattle, Washington, USA. [3]Institute of Medical Genetics, and [4]Department of Molecular Life Sciences, University of Zurich, Zürich, Switzerland. [5]Department of Genetics, King Faisal Specialist Hospital and Research Center, Riyadh, Saudi Arabia. [6]Department of Medical Genetics, Faculty of Medicine, Tehran University of Medical Sciences, Tehran, Iran. [7]Translational and Clinical Research Institute, Faculty of Medical Sciences, Newcastle University, Newcastle Upon Tyne, United Kingdom. [8]Department of Paediatric Neurology, Cambridge University Hospitals NHS Foundation Trust, Cambridge, United Kingdom. [9]Department of Human Genetics, Medical Research Institute, Alexandria University, Alexandria, Egypt. [10]The University of Washington Center for Mendelian Genomics is detailed in Supplemental Acknowledgments. [11]University of Washington Center for Mendelian Genomics, Seattle, Washington, USA. [12]Department of Genome Sciences, University of Washington, Seattle, Washington, USA. [13]The Genomics England Research Consortium is detailed in Supplemental Acknowledgments. [14]Medical Proteome Center, Institute for Ophthalmic Research, University of Tuebingen, Tuebingen, Germany. [15]Department of Anatomy and Cell Biology, College of Medicine, Alfaisal University, Riyadh, Saudi Arabia. [16]Center for Integrative Brain Research, Seattle Children's Research Institute, Seattle, Washington, USA.

Joubert syndrome (JBTS) is a recessive neurodevelopmental ciliopathy characterized by a pathognomonic hindbrain malformation. All known JBTS genes encode proteins involved in the structure or function of primary cilia, ubiquitous antenna-like organelles essential for cellular signal transduction. Here, we used the recently identified JBTS-associated protein armadillo repeat motif–containing 9 (ARMC9) in tandem-affinity purification and yeast 2-hybrid screens to identify a ciliary module whose dysfunction underlies JBTS. In addition to the known JBTS-associated proteins CEP104 and CSPP1, we identified coiled-coil domain containing 66 (CCDC66) and TOG array regulator of axonemal microtubules 1 (TOGARAM1) as ARMC9 interaction partners. We found that *TOGARAM1* variants cause JBTS and disrupt TOGARAM1 interaction with ARMC9. Using a combination of protein interaction analyses, characterization of patient-derived fibroblasts, and analysis of CRISPR/Cas9-engineered zebrafish and hTERT-RPE1 cells, we demonstrated that dysfunction of *ARMC9* or *TOGARAM1* resulted in short cilia with decreased axonemal acetylation and polyglutamylation, but relatively intact transition zone function. Aberrant serum-induced ciliary resorption and cold-induced depolymerization in *ARMC9* and *TOGARAM1* patient cell lines suggest a role for this new JBTS-associated protein module in ciliary stability.

Introduction

Ciliopathies are a heterogeneous class of disorders that arise from defects in the structure or function of the primary cilium (1, 2), a highly specialized microtubule-based sensory organelle that protrudes from the surface of most eukaryotic cell types (3). Joubert syndrome (JBTS) is a recessive, genetically heterogeneous neurodevelopmental ciliopathy defined by a distinctive brain malformation, recognizable as the "molar tooth sign" (MTS) (4) in axial MRIs through the midbrain-hindbrain junction. Affected individuals have hypotonia, ataxia, abnormal eye movements, and cognitive impairment. Additional features can occur, including retinal dystrophy, fibrocystic kidney disease, liver fibrosis, polydactyly, and coloboma (5). To date, variants in more than 35 genes have been causally linked to JBTS, but the genetic diagnosis cannot be identified in all patients, and the disease mechanisms remain unclear (6–8).

All JBTS-associated proteins identified thus far function in and around the primary cilium, but their dysfunction can affect a wide variety of cellular processes, including cilium formation, resorption, tubulin posttranslational modifications (PTMs), membrane phosphatidylinositol composition, ciliary signaling pathways, actin cytoskeleton dynamics, and DNA damage response signaling (9–14). Many JBTS proteins act together in complexes that localize to specific subdomains of the ciliary compartment. Disruption of the composition, architecture, or function of these ciliary subdomains causes disease (6).

The core of the cilium is composed of 9 microtubule doublets forming the ciliary axoneme, which is anchored to the cell by the

Authorship note: BLL, JCVDW, and TDSR contributed equally to this work and are co–first authors. RBG, RR, and DD contributed equally to this work.
Conflict of interest: The authors have declared that no conflict of interest exists.

Submitted: July 8, 2019; **Accepted:** May 14, 2020; **Published:** July 20, 2020.
Reference information: *J Clin Invest*. 2020;130(8):4423–4439.
https://doi.org/10.1172/JCI131656.

basal body, a modified centriole. The axonemal microtubules undergo a range of PTMs, including polyglutamylation and acetylation, that are important for the structure and function of the cilium (15–17). The ciliary membrane has a distinct protein and lipid distribution that differs from the contiguous plasma membrane. This unique composition is achieved in part by the transition zone (TZ) that connects the axoneme to the membrane and acts as a partition. Approximately half of the known JBTS proteins, including RPGRIP1L (JBTS7) (18, 19) and CC2D2A (JBTS9) (20), assemble into multiprotein complexes at the ciliary TZ, where they organize the molecular gate that regulates ciliary protein entry and exit (21); TZ dysfunction is thought to play a key role in JBTS (22). Another subset of JBTS-associated proteins, including ARL13B (JBTS8) (23) and INPP5E (JBTS1) (10), associate with the ciliary membrane distal to the TZ. These proteins are thought to regulate signaling pathways such as hedgehog (Hh) by modulating ciliary protein and lipid composition (24, 25). Different JBTS-associated proteins have been found to function at the basal body or ciliary tip (6). CSPP1 (JBTS 21) (26, 27) and CEP104 (JBTS25) (28) are mainly detected at the centrosomes and ciliary basal bodies; however, their exact molecular function and how defects in these proteins lead to JBTS are less well understood. CEP104 localizes to the ciliary tip during ciliogenesis, where it is required for structural integrity in the motile cilia of *Chlamydomonas* and *Tetrahymena* (29, 30). Pathogenic variants in the gene encoding the ciliary tip kinesin KIF7 (JBTS12) also cause JBTS, and KIF7 dysfunction has been linked to defects in tubulin acetylation and Hh signaling (31).

Recently, we identified biallelic pathogenic armadillo repeat motif–containing 9 (*ARMC9*) variants in individuals with JBTS (JBTS30). ARMC9 localizes to centrioles (32) and the proximal portion of the cilium (33) in mammalian cilia. *ARMC9* transcript levels are upregulated with induction of ciliogenesis, and *armc9* dysfunction in zebrafish yields typical ciliopathy phenotypes (32). ARMC9 has not been identified as a component of the ciliary JBTS–associated protein complexes mentioned above, so in this work, we used ARMC9 as bait in protein interaction screens. These screens identified a microtubule-associated ciliary protein module containing multiple other JBTS-associated proteins (CEP104, CSPP1, RPGRIP1L, and CEP290) and 2 other ciliary proteins (TOG array regulator of axonemal microtubules 1 [TOGARAM1] and coiled-coil domain containing 66 [CCDC66]) not previously implicated in JBTS. Strikingly, we identified biallelic pathogenic *TOGARAM1* variants as the cause of JBTS in 5 families. To decipher the function of the ARMC9-TOGARAM1 protein module and assess its role in the pathology of JBTS, we mapped the interaction domains and evaluated cellular defects in cultured human cells and zebrafish mutants. We found that these proteins, previously shown to associate with microtubules (29, 34–36), were required for appropriate PTM of ciliary microtubules and cilium stability.

Results

Identification of a protein module implicated in JBTS. We performed protein interaction screens to define the ARMC9-associated interactome. To identify direct binding partners, we used full-length ARMC9 and 4 fragments (Figure 1A) as bait in a GAL4-based yeast 2-hybrid (Y2H) interaction trap screen of 2 validated prey retinal cDNA libraries that were generated via random or oligo-dT primers (37). Using full-length ARMC9 as a bait, we identified 4 proteins previously implicated in ciliary function as binary interactors, including ARMC9 itself (suggesting a propensity to multimerize), TOGARAM1 (29, 34), CCDC66 (36, 38), and the JBTS-associated protein CSPP1 (39). Validation of these interactions and evaluation of the interacting domains was performed by Y2H coexpression. This assay indicated that the potential self-binding propensity of ARMC9 is mediated by fragment 2 containing the N-terminal 350-aa stretch containing the lissencephaly type 1–like homology motif (LisH) and coiled-coil (CC) domains, whereas TOGARAM1 and CSPP1 associated with fragment 4 (150–665 aa) containing the CC domain and the armadillo repeats (ARM) domain (Figure 1, B and C). We also used full-length TOGARAM1 and 3 fragments (Figure 1D) in parallel screens, which confirmed the direct interaction between TOGARAM1 and ARMC9 (Figure 1E) and yielded an additional candidate interactor, the JBTS-associated TZ protein RPGRIP1L (JBTS7) (Figure 1E). The interaction with ARMC9 was mapped to the N-terminal portion of TOGARAM1 (fragment 1) containing the TOG1 and TOG2 domains, whereas RPGRIP1L bound to the linker region (fragment 2) between the TOG2 and TOG3 domains (Figure 1E).

To identify ARMC9-associated protein complexes, we expressed strep–Flag epitope–tagged ARMC9 in HEK293T cells, followed by tandem affinity purification (TAP) and subsequent mass spectrometry. We identified 106 candidate ARMC9 interactors, including TOGARAM1 and the JBTS-associated protein CEP290 (Figure 1, G and H; Supplemental Table 1; supplemental material available online with this article; https://doi.org/10.1172/JCI131656DS1). Subsequent TAP experiments using tagged TOGARAM1, CCDC66, and CSPP1 confirmed the presence of ARMC9 in the TOGARAM1 and CCDC66 complexes and extended the network to include several other ciliary proteins (Supplemental Tables 2–4). For TOGARAM1, these additional candidate interactors included the ciliary proteins ARMC9, CEP104, IFT74, IFT172, PLK1, and PRPF31 (Supplemental Table 2); for CCDC66, they included ARMC9 and DYNLL1 (Supplemental Table 3); and for CSPP1, they included RPGRIP1L and CEP290 (Supplemental Table 4).

To further validate the ARMC9 interactors identified in TAP and Y2H experiments and evaluate their propensity to interact, we performed reciprocal co-IPs of all binary permutations of the module components ARMC9, TOGARAM1, CEP104, CCDC66, and CSPP1 (Figure 1F and Supplemental Figure 1, A–I). The results confirmed the interaction of ARMC9 with TOGARAM1, CCDC66, CEP104, and CSPP1 (Figure 1G). Additionally, we performed PalmMyr-CFP mislocalization assays to further confirm the interaction of TOGARAM1 and ARMC9. The PalmMyr-CFP assay uses a PalmMyr tag, which provides sites for palmitoylation and myristoylation. The palmitoylation and myristoylation force the tagged protein to (mis)localize to the cell membrane (40). This mislocalization can be evaluated by fluorescence microscopy of cyan fluorescent protein (CFP) signal. We transfected PalmMyr-CFP–tagged ARMC9 and monomeric red fluorescent protein–tagged (mRFP-tagged) TOGARAM1 into human telomerase reverse transcriptase–retinal pigmented epithelium (hTERT-RPE1) cells, alone

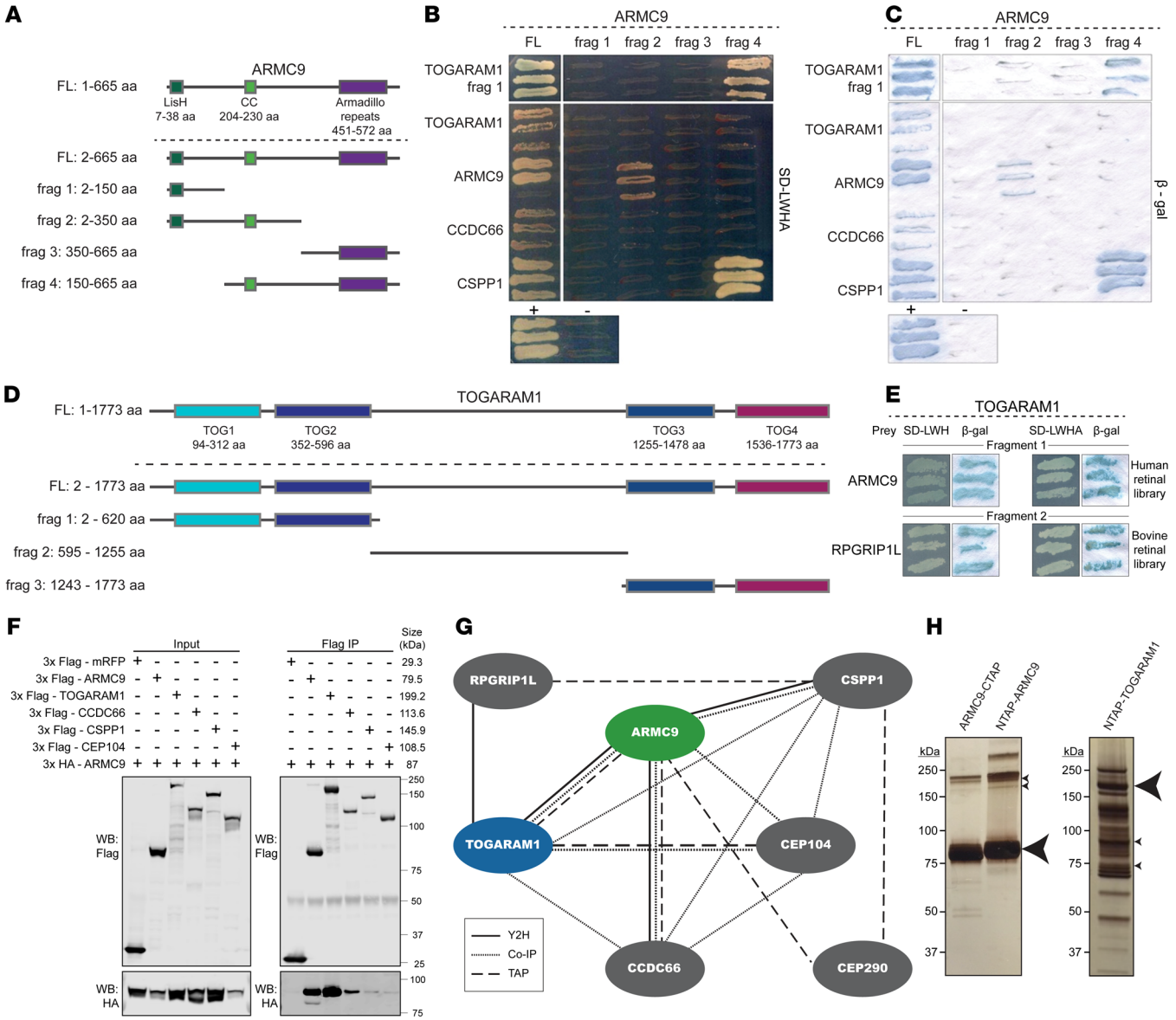

Figure 1. ARMC9 associates with TOGARAM1 in a ciliary module. (**A**) Schematic of full-length ARMC9 and fragments (frag) used as baits in Y2H bovine and human retinal cDNA library screens. The domains indicated are the predicted LisH (dark green), coiled-coil (CC) domain (light green), and the ARM-containing domain (purple). (**B**) Direct interaction analysis grid using full-length prey constructs. Selection of strains coexpressing bait and prey constructs was performed on quadruple-knockout medium (synthetic defined lacking leucine, tryptophan, histidine, and adenine [SD-LWHA]). The top row displays yeast colony growth when using fragment 1 of TOGARAM1 as prey. (**C**) β-Gal activity assay confirming the interactions. (**D**) Schematic of full-length TOGARAM1 and fragments used in Y2H bovine and human retinal cDNA screens. (**E**) TOGARAM1 screen results validated in a Y2H-directed interaction analysis on triple-knockout (SD-LWH) and quadruple-knockout (SD-LWHA) media. (**F**) Flag co-IP of 3xFlag-ARMC9, 3xFlag–TOGARAM1, 3xFlag-CCDC66, 3xFlag-CSPP1, and 3xFlag-CEP104 with 3xHA-ARMC9. 3xFlag-mRFP served as a negative control. Western blot (WB) analysis after Flag-tag purification indicated the presence of 3xHA-ARMC9, confirming the interactions. 3xFlag-mRFP showed no interaction with 3xHA-ARMC9. (**G**) ARMC9 interacted with TOGARAM1, as confirmed by TAP (dashed lines) and Y2H (solid lines) screens. Validation was subsequently performed using co-IP (dotted lines). (**H**) Silver stain gels of C-terminally and N-terminally Strep/Flag tandem affinity purification–tagged (SF-TAP–tagged) ARMC9 (left, large arrowhead, 80 kDa) and N-terminally SF-TAP–tagged TOGARAM1 (right, large arrowhead, 200 kDa) after protein purification. The small arrows indicate the expected protein bands of 2 TOGARAM1 isoforms (195.6 kDa and 189.4 kDa) in the ARMC9 TAP purification, and 2 endogenous ARMC9 isoforms (91.8 kDa and 75.7 kDa) in the TOGARAM1 TAP purification. FL, full-length.

and in combination, to assess the interaction between ARMC9 and TOGARAM1. Cells transfected with PalmMyr-CFP-ARMC9 alone showed diffuse localization across the cell membrane (Supplemental Figure 1J), whereas mRFP-TOGARAM1 alone localized to microtubule-like structures (Supplemental Figure 1K). Coexpression yielded complete colocalization along these structures despite the PalmMyr tag on ARMC9 (Supplemental Figure 1L), thus indicating a direct interaction of the 2 proteins and a likely strong microtubule-binding affinity of TOGARAM1.

TOGARAM1 variants cause JBTS in humans. Next, we investigated whether our interactome data set could be used to identify new JBTS-associated genes. We cross-referenced the ARMC9

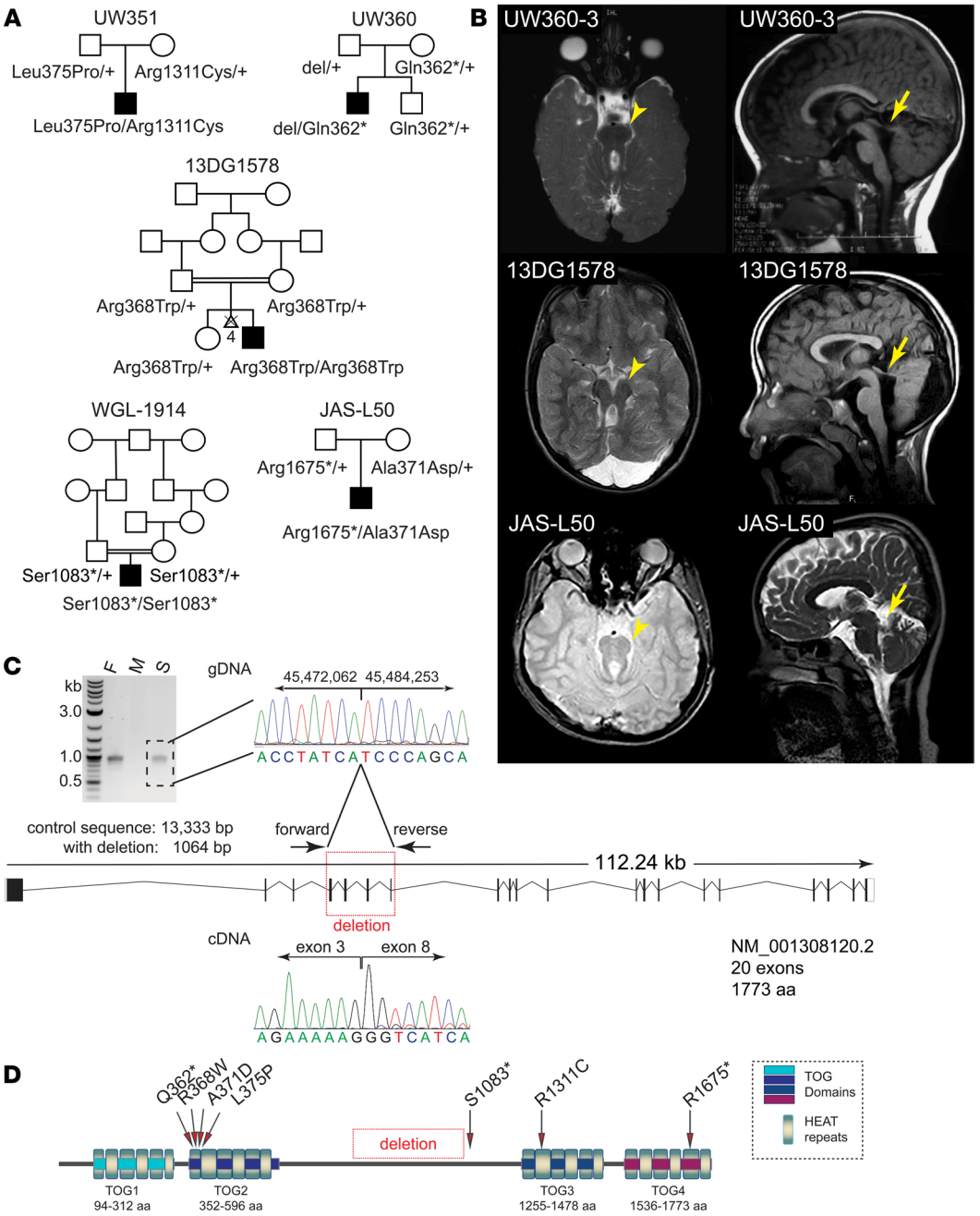

Figure 2. *TOGARAM1* variants cause JBTS. (**A**) Pedigrees and segregation of *TOGARAM1* variants. (**B**) Brain imaging features in individuals with *TOGARAM1*-related JBTS. MTS (arrowheads in left column, axial T2-weighted images) and elevated roof of the fourth ventricle (arrows in right column, sagittal T1-weighted [top 2] and T2-weighted [bottom] images). Much of the cerebellar tissue on the sagittal images (right panels) is hemisphere, based on axial and coronal views (not shown). (**C**) Multi-exon deletion in UW360. Primers flanking the predicted deletion amplify a 1064-bp product in the father (F) and the affected son (S) due to a 12,191-bp deletion, but not in the mother (M), because the predicted product was too large. Sanger sequencing of the breakpoint in gDNA (upper) and cDNA (lower) from the affected child confirmed the deletion of exons 4–7. Coding genomic schematic of *Homo sapiens TOGARAM1*. Transcript variant 1 is shown (NM_001308120.2; variant 2 NM_015091.4, not shown). (**D**) Protein schematic of TOGARAM1 with JBTS-associated variants indicated. TOG domains 1–4 are shown, with HEAT repeats indicated in gradients of blue.

interactome data with DNA sequence data from our cohort of more than 600 families affected by JBTS (41). We first evaluated exome sequence data for 53 individuals in 51 families without variants in known JBTS genes. We identified biallelic, missense *TOGARAM1* variants in a fetus with cerebellar vermis hypoplasia and polydactyly (UW351-3 in Figure 2A and Table 1). These variants (c.1124T>C; p.Leu375Pro and c.3931C>T; p.Arg1311Cys) are rare in gnomAD, version 2.1 (http://gnomad.broadinstitute.org) (42) and predicted to be deleterious by combined annotation-dependent depletion (CADD) (43) (Table 1). To identify additional families, we sequenced all of the known JBTS genes using small-molecule molecular inversion probe capture (44) in 534 additional

Table 1. Variants and clinical features in individuals with *TOGARAM1*-related JBTS

	UW351-3	UW360-3	13DG1578	WGL-1914	JAS-L50
Variant 1[A]	c.1124T>C; p.(Leu375Pro)	c.1084C>T; p.(Gln362*)	c.1102C>T; p.(Arg368Trp)	c.3248C>A; p.(S1083*)	c.1112C>A; p.(Ala371Asp)
Allele frequency 1[B]	8/276914	0/251328	0/251284	0	5/282580
CADD, v1.3[C]	25.5	35	28.7	38	26.6
Parent	Father	Mother	NA	NA	Mother
Variant 2[A]	c.3931C>T; p.(Arg1311Cys)	del14q21.2: g.45472062-45484253	c.1102C>T; p.(Arg368Trp)	c.3248C>A; p.(Ser1083*)	c.5023C>T; p.(Arg1675*)
Allele frequency 2[B]	0/218738	NA	0/251284	0	1/251414
CADD, v1.3[C]	35	NA	28.7	38	NA
Parent	Mother	Father	NA	NA	NA
Ethnicity/country	Mixed European (Australia)	Mixed European (United States)	Middle Eastern (Egypt)	Middle Eastern (Iran)	White British
Sex	Male	Male	Male	Male	Female
Age	21-wk fetus	16 yr	11 yr, 5 mo	6 yr	14 yr
Molar tooth	VH	Yes	Yes	Yes	Yes
Dev disability	NA	Yes	Yes	Yes	Yes
Apnea/tachypnea	NA	No	Yes	NA	NA
Abnl eye mvts	NA	Y (and strabismus)	Yes	NA	Yes
Retinal	NA	No	No	NA	No
Kidney	NA	No	No	Yes	Yes
Liver	NA	No	No	Yes	No
Polydactyly	Y (B post-ax foot)	No	No	Y (B post-ax hand)	No
Coloboma	NA	No	No	Yes	No
Craniofacial	Broad nasal bridge, posteriorly rotated ears, thickened neck	Low-set ears, high, arched palate	Broad nose, anteverted alae, deep-set eyes, hypertelorism, metopic ridge, frontal bossing, low-set ears	Broad nasal bridge, anteverted alae, deep set eyes, hypertelorism, frontal bossing	Oculomotor apraxia, bilateral ptosis, left jaw/wink ptosis
Other		Widely spaced nipples, undescended testes, possible micropenis	Widely spaced nipples, small scrotum and testes	Corpus callosum hypoplasia, neonatal metabolic acidosis and jaundice, hepatomegaly, cholestasis, bilateral hydronephrosis hypotrichosis, small scrotum and testes, possible micropenis, microphthalmia, coloboma	Short stature, generalized hypotonia, lumbar hyperlordosis, obesity, joint hypermobility, nonverbal, autistic behaviors, small, scarred left kidney

[A]NM_015091.2; [B]gnomAD reference; [C]CADD reference. Abnl, abnormal; B, bilateral; Dev, developmental; mvts, movements; NA, not available; post-ax, post-axial; VH, vermis hypoplasia.

individuals from the same cohort and identified another individual (UW360-3 in Table 1 and Figure 2A) with the MTS (Figure 2B) and a nonsense variant (c.1084C>T; p.Gln362*) on 1 allele and low read depth indicating a possible multi-exon deletion event on the other allele. We confirmed a 12-kb deletion using a custom comparative genomic hybridization array, and fibroblast cDNA sequencing revealed deletion of exons 4–7 (Figure 2C). Genomic DNA sequencing of the proband and parents revealed that the 12,191-bp deletion was inherited from the father (Figure 2C). In parallel, exome sequencing in several other cohorts of individuals with ciliopathy and neurodevelopmental conditions identified 3 other individuals with *TOGARAM1*-related JBTS (Table 1 and Figure 2, A and B): 13DG1578 (consanguineous) with a homozygous rare, predicted deleterious missense variant (c.1102C>T; p.Arg368Trp); WGL-1914 (consanguineous) with a rare, homozygous stop-gain variant (c.3248C>A; p.Ser1083*); and JAS-L50 (nonconsanguineous) with rare, compound heterozygous missense and stop-gain variants (c.1112C>A; p.Ala371Asp and c.5023C>T; p.Arg1675*). Most variants identified in this work cluster around the tumor overexpressed gene (TOG) domains in the protein (Figure 2D). TOGARAM1 is also known as FAM179B and KIAA0423, with homologs CHE-12 in *Caenorhabditis elegans* and crescerin-1 in mouse. Segregation analysis for all affected families confirmed a recessive inheritance pattern (Figure 2A and Supplemental Figure 3).

The 5 affected individuals had features consistent with JBTS, including classic brain imaging findings (absent cerebellar vermis and thick, horizontally oriented superior cerebellar peduncles, giving the appearance of the MTS) in the 4 children (Figure 2B), and cerebellar vermis hypoplasia in the fetus (UW351-3). This fetus also had bilateral postaxial foot polydactyly and abnormal

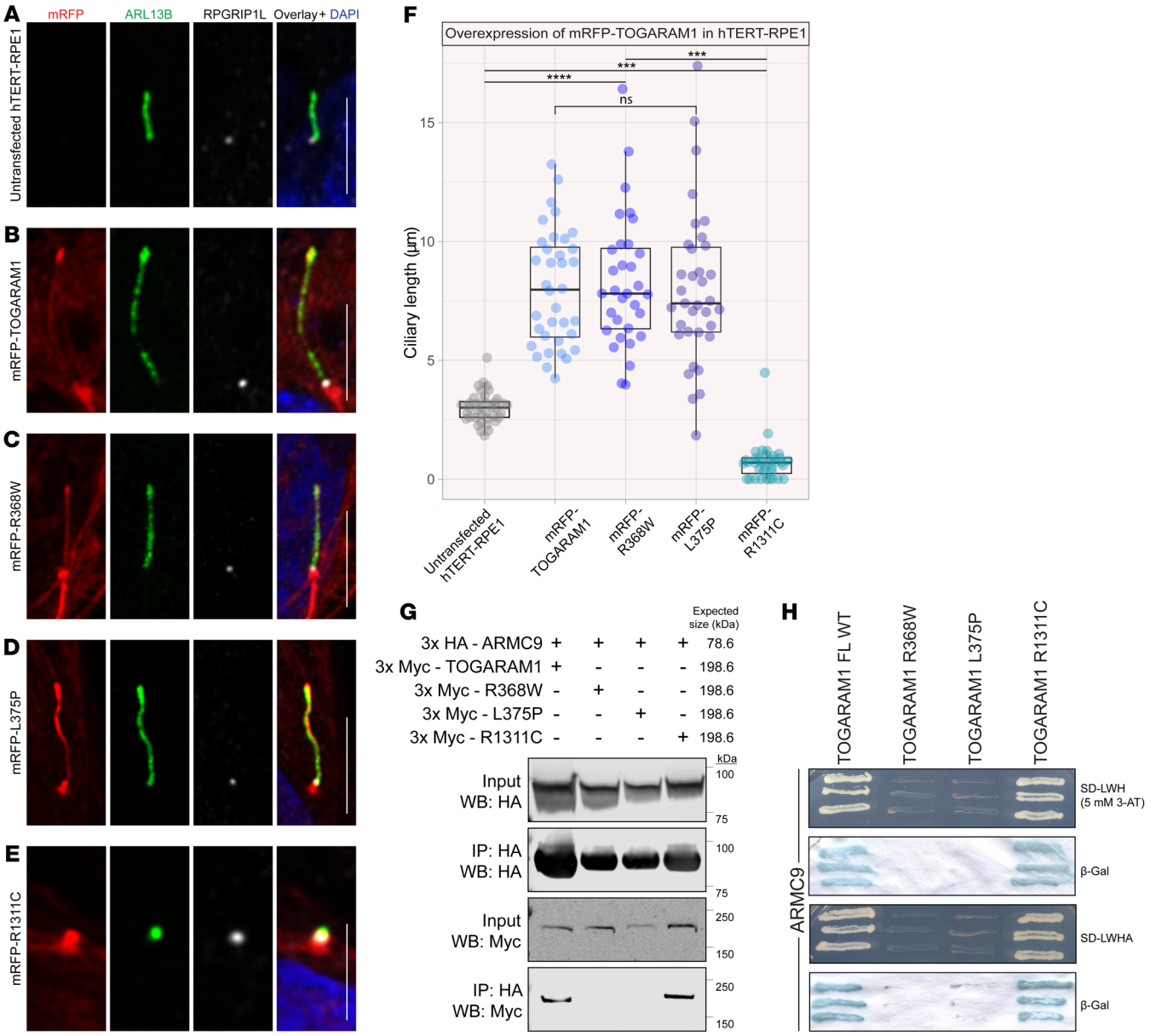

Figure 3. Overexpression of TOGARAM1 affects ciliary length, and TOG2 domain variants reduce ARMC9 interaction. (**A**) Images of untransfected control hTERT-RPE1 cells. The cilium is shown with the TZ marker RPGRIP1L (white) and the ciliary membrane marker ARL13B (green). Scale bar: 5 µm. (**B**–**E**) Transient mRFP-TOGARAM1 overexpression (red) in hTERT-RPE1 cells shown with the TZ marker RPGRIP1L (white) and the ciliary membrane marker ARL13B (green). (**B**) WT mRFP-TOGARAM1 (mRFP-TOGARAM1), (**C**) mRFP-TOGARAM1-Arg368Trp (mRFP-R368W), (**D**) mRFP-TOGARAM1-Leu375Pro (mRFP-L375P), and (**E**) mRFP-TOGARAM1-Arg1311Cys (mRFP-R1311C). Images are representative of more than 30 cilia assessed per condition over 3 experiments. Scale bars: 5 µm (**B**–**E**). (**F**) Quantification of cilium lengths with overexpression of WT and variant forms of mRFP-TOGARAM1 (untransfected $n = 39$, WT $n = 36$, Arg368Trp $n = 32$, Leu375Pro $n = 35$, Arg1311Cys $n = 36$). Box plot horizontal bars represent the median ± 95% CI. $P > 0.05$ (NS), $^{***}P \le 0.001$, and $^{****}P \le 0.0001$, by 1-way ANOVA with Tukey's multiple comparisons test. No significant differences were found between cells overexpressing mRFP-TOGARAM1, mRFP-Arg368Trp, and mRFP-Leu375Pro. $P = 0.0004$ for untransfected versus Arg1311Cys. (**G**) Co-IP of HA-tagged ARMC9 and Myc-tagged TOGARAM1: WT and Myc-tagged TOGARAM1-Arg1311Cys interacted with ARMC9, whereas the TOGARAM1 variants Arg368Trp and Leu375Pro did not. (**H**) Y2H direct interaction analysis assay with ARMC9 and TOGARAM1: WT and TOGARAM1-Arg1311Cys interacted with ARMC9, whereas the TOGARAM1 variants Arg368Trp and Leu375Pro did not. 3-AT, 3-amino-1,2,4-triazole.

craniofacial features at autopsy, including a broad nasal bridge and posteriorly rotated ears. The 4 living children have typical hypotonia, ataxia, cognitive delays, and behavioral features associated with JBTS, whereas WGL-1914 and JAS-L50 had kidney involvement, and WGL-1914 also had liver involvement. Uncommonly seen in individuals with JBTS, we noted widely spaced nipples, male genital abnormalities (undescended testicles and possible micropenis in UW360-3, and small scrotum and testicle in 13DG1578), and somewhat similar dysmorphic features in several of these individuals (Table 1).

JBTS-associated TOGARAM1 missense variants in the TOG2 domain disrupt ARMC9-TOGARAM1 interaction. TOGARAM1 is a member of the highly conserved FAM179 protein family and is found across ciliated eukaryotes including *Chlamydomonas rein-*

hardtii, *Tetrahymena thermophila*, and *C. elegans*. TOGARAM1 has 4 conserved TOG domains that show similarity to the tubulin-binding domains in ch-TOG and CLASP family proteins (34). Arg368Trp, Ala371Asp, and Leu375Pro lie within the highly conserved TOG2 domain (Figure 2D and Supplemental Figure 2A), which has been found to promote microtubule polymerization in vitro (34). The TOG2 domain conforms to the canonical TOG domain architecture found in other TOG array–containing proteins such as CLASP and Stu2 (Supplemental Figure 2A), therefore, disruption of this domain is predicted to disturb microtubule binding (45). Using in silico analysis of the effects of point mutations, we found that Arg368Trp, Ala371Asp, and Leu375Pro variants were predicted to be deleterious to protein structure (45). Residue 368 is highly conserved, and modeling the WT and mutant TOG domains using HOPE (http://www.cmbi.umcn.nl/hope/) (45) predicted that the larger and neutral tryptophan would disrupt the normal hydrogen bonds with the aspartic acid residues at positions 361 and 405**)** (Supplemental Figure 2, C and D). Position 371 is highly conserved, and because of the difference in size and hydrophobicity, aspartic acid at this position is predicted to disrupt the structure and function of the HEAT4 domain (Supplemental Figure 2, E and F). Position 375 is located in a predicted α-helix and is highly conserved; proline at this position is predicted to disrupt this α-helix as it introduces a bend in the polypeptide chain (Supplemental Figure 2, G and H), likely affecting protein folding or interaction with other domains (45).

To assess the effects of JBTS-associated missense variants, we modeled 2 of the TOG2 domain variants (Arg368Trp and Leu375Pro) and the single TOG3 domain variant (Arg1311Cys) by expressing WT and mutant mRFP-tagged TOGARAM1 in control (Figure 3, A–E) and genetically edited *TOGARAM1*-mutant hTERT-RPE cell lines (Supplemental Figure 4, A and B). The genetically edited *TOGARAM1*-mutant hTERT-RPE cell line *TOGARAM1* mut 1 has a biallelic deletion of the ATG site of TOGARAM1 (Supplemental Figure 5, A and B). Overexpressed WT TOGARAM1 localized along the ciliary axoneme and was associated with markedly longer cilia compared with that seen in untransfected WT cells (Figure 3, A and B) and *TOGARAM1* mut 1 cells (Supplemental Figure 4, AB). Exogenous TOGARAM1 harboring these 3 variants individually also localized to the cilium, but overexpression of the TOG2 domain variants Arg368Trp and Leu375Pro resulted in longer cilia, whereas overexpression of the TOG3 domain variant Arg1311Cys resulted in shorter cilia compared with untransfected cells (Figure 3, A–E, quantification in Figure 3F). These data suggest that disruption of the TOG3 domain may have a dominant-negative effect on the microtubule polymerization capacity of TOGARAM1 and that disruption of the TOG3 domain has a different effect on TOGARAM1 localization and ciliary extension compared with TOG2 domain variants.

We next investigated the effects of the *TOGARAM1* variants on the interaction with ARMC9 using co-IP, binary Y2H interaction analysis, and PalmMyr colocalization assays. We found that the variants in the TOG2 domain (Arg368Trp and Leu375Pro) abolished co-IP of HA-ARMC9 with Myc-TOGARAM1, whereas the Arg1311Cys variant in the TOG3 domain did not influence the interaction in these assays (Figure 3G). Y2H analysis confirmed these binary interactions (Figure 3H). In PalmMyr assays, the individually expressed WT and mutant mRFP-tagged TOGARAM1 proteins localized along the length of cilia and along cytoplasmic microtubules (Supplemental Figure 4D). Coexpression of PalmMyr-CFP–tagged ARMC9 with WT or Arg1311Cys mRFP-TOGARAM1 resulted in a pattern consistent with colocalization to cytoplasmic microtubules (Supplemental Figure 4E), indicating protein-protein interaction. In contrast, coexpression with the TOG2 variants resulted in PalmMyr-CFP–tagged ARMC9 remaining localized to the plasma membrane, suggesting a lack of interaction with the TOGARAM1 mutants affecting the TOG2 domain (Supplemental Figure 4E). Taken together, these data indicate that variants in the TOG2 domain abrogate ARMC9-TOGARAM1 interaction.

togaram1 mutations cause ciliopathy phenotypes in zebrafish. To further investigate the function of TOGARAM1 and the association between TOGARAM1 dysfunction and JBTS, we turned to zebrafish, an established model organism for ciliopathies. Indeed, zebrafish display a variety of ciliated cell types similar to those in humans, and pathogenic variants in human ciliopathy genes result in typical ciliopathy phenotypes in zebrafish. Ciliated cells typically assessed in the zebrafish model include epithelial cells in pronephric (kidney) ducts, olfactory neurons in nose pits, or neuronal progenitors on larval brain ventricular surfaces.

We identified a single zebrafish *togaram1* ortholog displaying a highly conserved C-terminal region encompassing 2 TOG domains (similar to human TOG3 and TOG4) and a single N-terminal TOG domain corresponding to the mammalian TOG2 domain (Supplemental Figure 6A). The 3 TOG domains are well conserved between zebrafish and its corresponding human counterparts (50%–58% aa identity and 72%–77% similarity). As for the linker region between TOG domains, although it is more poorly conserved, it is enriched in serines and lysines (125 of 589 residues are Ser or Lys), similar to the proportion found in the human protein (165 of 657 residues are Ser or Lys); this is a common feature of TOG domain–containing proteins (46). Gene Synteny analysis (http://syntenydb.uoregon.edu/synteny_db/) confirmed that the identified zebrafish sequence represents the ortholog of human *TOGARAM1* (Supplemental Figure 6B). Importantly, on the paralogous chromosomal fragment generated by the teleost-specific whole-genome duplication, no second *togaram1* paralog could be identified. Moreover, Synteny analysis also revealed that the zebrafish genome lacks a *TOGARAM2* ortholog (Supplemental Figure 6C), leaving zebrafish with just 1 *togaram* ortholog. These findings support the utility of zebrafish as a model for *TOGARAM1*-associated human disease.

We next generated zebrafish mutants using CRISPR/Cas9. Two different pairs of sgRNAs targeting different regions of the gene (Supplemental Figure 6D) led to similar phenotypes in injected F0 larvae. We noted that 39% developed a curved body shape and 9% developed kidney cysts, both typical zebrafish ciliopathy–associated phenotypes (Supplemental Figure 6E). Genotyping of single larvae revealed a very high mutation efficiency (94% of sequenced clones from 7 larvae had small insertions-deletions, the majority of which were frameshift mutations). Mutant F0 fish displayed a striking scoliosis phenotype as juveniles (Supplemental Figure 6E), reminiscent of other ciliopathy mutants including *armc9* CRISPR-F0 fish (32). Taken together, these results confirm that loss of *togaram1* causes ciliopathy phenotypes in zebrafish and support a role for *togaram1* in ciliary function.

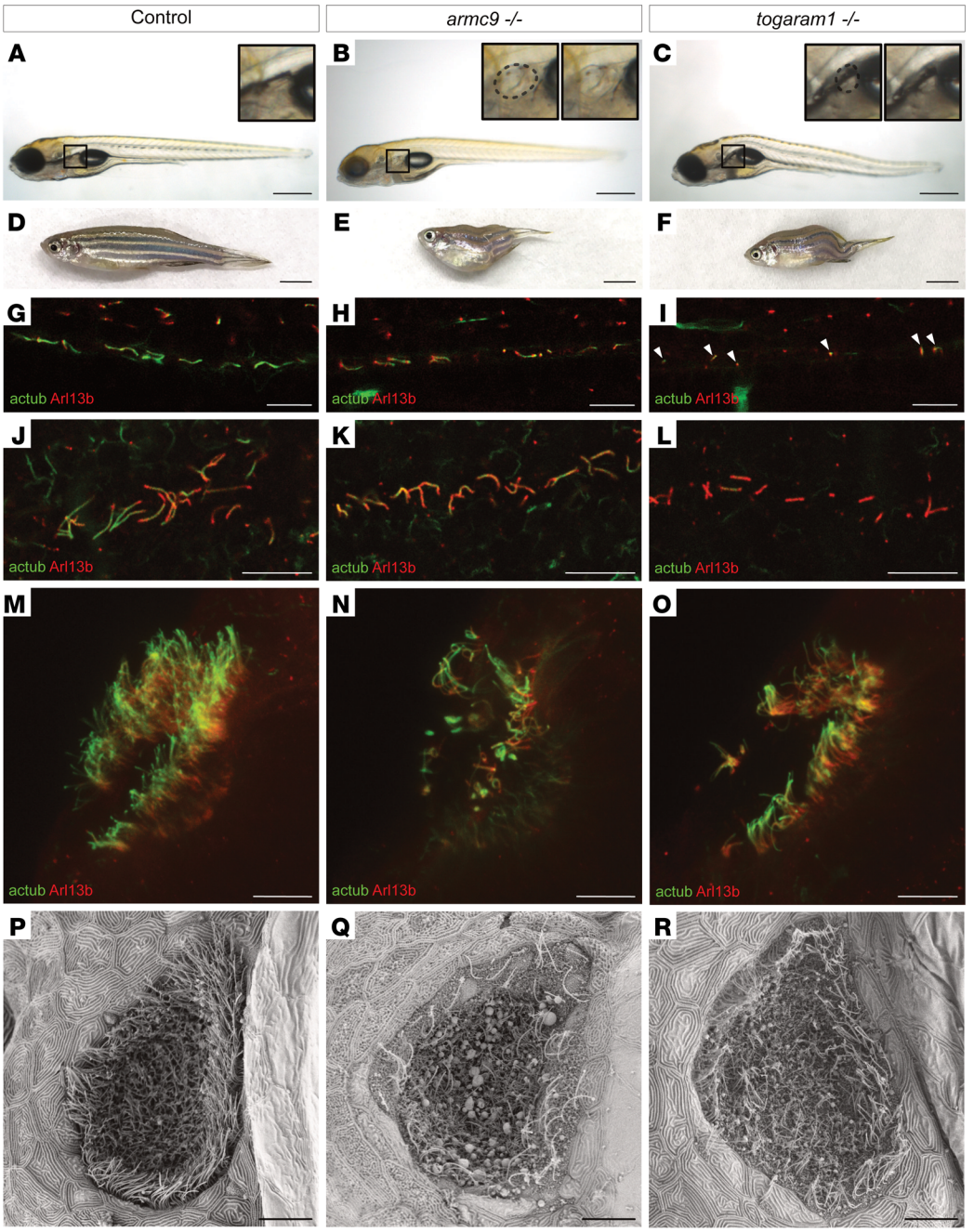

Figure 4. *armc9*- and *togaram1*-mutant zebrafish display ciliopathy-associated phenotypes. (**A**–**C**) Larval phenotype demonstrating kidney cysts in *armc9*$^{-/-}$ (**B**) and kidney cysts and a curved body shape in *togaram1*$^{-/-}$ (**C**) larvae. Black boxes in **A**–**C** show ×3.5 magnification of the glomerulus region in the inset. Dashed lines highlight the kidney cysts in **B** and **C**. (**D**–**F**) Adult scoliosis phenotype in both mutants (**E** and **F**) compared with WT (**D**). (**G**–**I**) Immunofluorescence of the pronephric duct in 3-dpf larvae showing fewer cilia. White arrowheads in **I** point to the short remaining cilia in the *togaram1* mutant. (**J**–**L**) Immunofluorescence of midbrain ventricles showed shortened cilia in 3-dpf *armc9*- and *togaram1*-mutant zebrafish larvae (**K** and **L**). (**M**–**O**) Immunofluorescence of 3-dpf zebrafish nose pits showed decreased cilia numbers in both mutants (**N** and **O**) compared with WT (**M**). (**P**–**R**) Scanning electron microscopy of 5-dpf zebrafish nose pits confirmed the reduced cilia numbers in *armc9*$^{-/-}$ (**Q**) and *togaram1*$^{-/-}$ (**R**) larvae. The controls were WT, +/+, or +/– siblings of –/–. Scale bars: 500 μm (**A**–**C**), 5 mm (**D**–**F**) and 10 μm (**G**–**R**).

armc9- and togaram1-mutant zebrafish display similar phenotypes. To further evaluate the link between *TOGARAM1* and *ARMC9*, we compared zebrafish mutants in the 2 genes. Following up on our previous work (32), we raised several stable (>F2) zebrafish lines harboring frameshift insertion and deletion alleles of *armc9* (Supplemental Figure 6F). Since homozygous mutants from all generated alleles have comparable phenotypes, we focused on the *armc9*^{zh505} allele for follow-up experiments (Supplemental Figure 6F). This allele harbors a 110-bp insertion in exon 14 that leads to exon skipping, causing a frameshift that

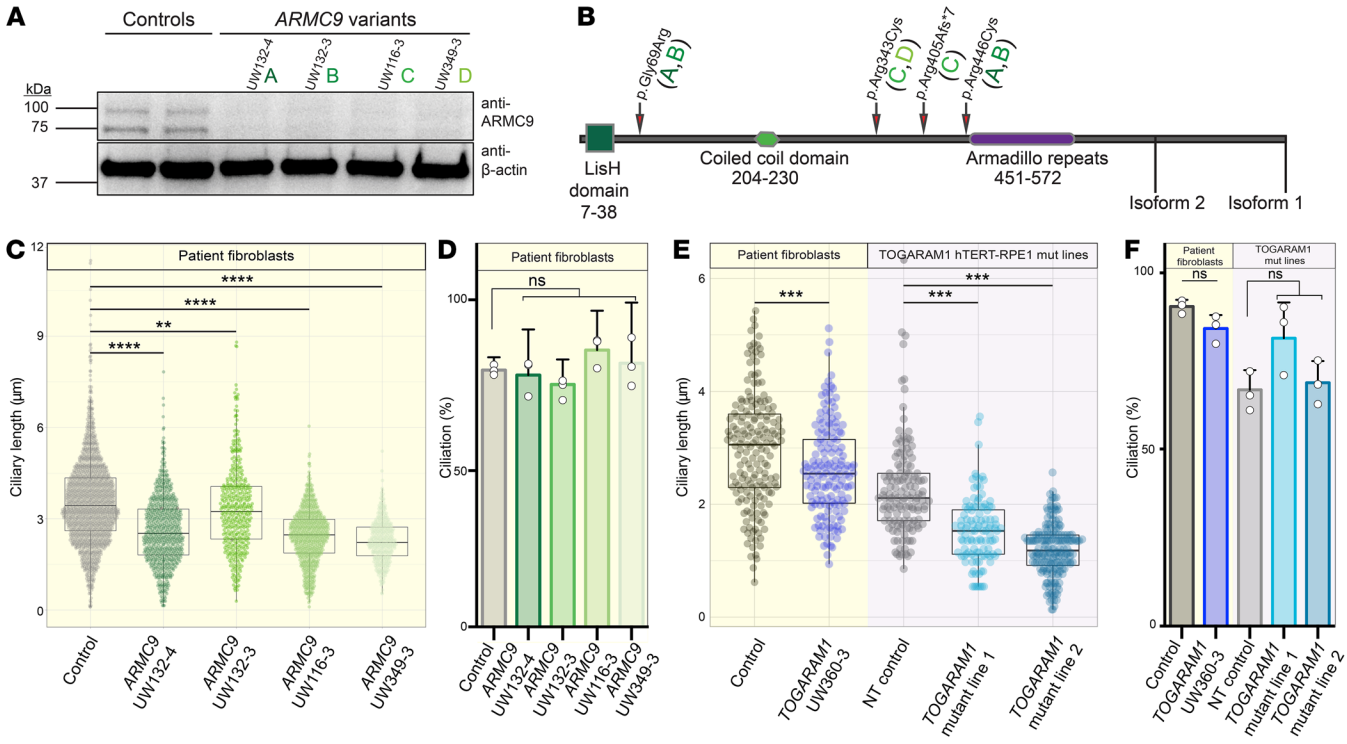

Figure 5. ARMC9 and TOGARAM1 dysfunction results in short cilia. (**A**) Immunoblot of endogenous ARMC9 in control and patient fibroblasts indicating trace amounts of ARMC9 isoforms 1 and 2 (92 and 75.5 kDa). β-Actin was used as a loading control. (**B**) ARMC9 schematic indicating JBTS-associated patient variants (green letters represent the variants found in the patients indicated in **A**). (**C**) Ciliary length in control and *ARMC9* patient fibroblasts (control n = 1395, UW132-4 n = 699, UW132-3 n = 437, UW116-3 n = 656, and UW349-3 n = 353). Significance was assessed by 1-way ANOVA with Dunnett's multiple testing correction. (**D**) Ciliation percentage in *ARMC9* fibroblast lines (control n = 1723, UW132-4 n = 898, UW132-3 n = 584, UW116-3 n = 764, and UW349-3 n = 425). Results were not significant using a Kruskal-Wallis test. (**E**) Ciliary length in control and *TOGARAM1* patient fibroblasts (yellow panel). P = 0.0003, by unpaired Student's t test. hTERT-RPE1 cilia length in WT and *TOGARAM1*-mutant lines (purple panel) based on ARL13B staining. More than 100 cilia were pooled from 2 experiments (control n = 137, *TOGARAM1*-mutant line 1 n = 111, and *TOGARAM1*-mutant line 2 n = 178). $P < 0.0001$, by 1-way ANOVA with Dunnett's multiple corrections test. (**F**) Ciliation percentage in *TOGARAM1* patient fibroblasts (yellow panel: control n = 466 and UW360-3 n = 429 over 3 experiments). The results were not significant using a Mann-Whitney U test. The ciliation percentage in engineered *TOGARAM1*-mutant hTERT-RPE1 cells (purple panel: control n = 330, *TOGARAM1*-mutant line 1 n = 363, and *TOGARAM1*-mutant line 2 n = 357 over 3 experiments) Results were not significant using the Kruskal-Wallis test. White circles represent individual experiments from **D** and **F**. Box-and-whisker plots in **C** and **E** represent the median, with the 95% CI indicated by the notches. All ciliary length measurements were based on ARL13B staining. $P > 0.05$ (NS), $^{**}P \le 0.01$, $^{***}P \le 0.001$, and $^{****}P \le 0.0001$.

inserts a stop codon at position 73 of exon 15. *armc9*$^{-/-}$ larvae had a straight body shape and an incompletely penetrant pronephric cyst phenotype affecting 44% of the homozygous mutants (Figure 4, A and B). In comparison, *togaram1*^{zh509}- or *togaram1*^{zh510}-mutant F2 larvae harboring frameshift mutations leading to a stop codon in exon 23 had a slightly curved body shape and displayed a similar rate of kidney cysts compared with *armc9*$^{-/-}$ mutants (Figure 4C). Pronephric cysts and body curvature do not necessarily correlate with each other in *togaram1* mutants, as each phenotype can be found in isolation or in combination, but overall, 85% of *togaram1*$^{-/-}$ larvae have at least 1 ciliopathy phenotype. Neither mutant showed heart laterality defects that are seen in some zebrafish ciliopathy models. In addition to frameshift mutations in exons 21 and 22, we also identified a 21-bp in-frame deletion leading to loss of 7 aa in the TOG4 domain, 6 of which were highly conserved (*togaram1*^{zh508}, Supplemental Figure 7). Homozygous in-frame mutant larvae were indistinguishable from the frameshift mutants, suggesting that the TOG4 domain may be critical for Togaram1 function.

In addition to the pronephric cysts, both *armc9*$^{-/-}$ and *togaram1*$^{-/-}$ fish developed scoliosis as juveniles compared with the WT fish (Figure 4, D–F), as previously described in other zebrafish ciliary mutants (47, 48). Given that pronephric cysts and curved bodies are typical ciliopathy phenotypes, we next analyzed the cilia in both mutants using immunofluorescence with anti-Arl13b and anti-acetylated α-tubulin antibodies. Compared with WT, larvae of both mutants had reduced numbers of shortened pronephric, ventricular, and nose pit cilia (Figure 4, G–O), the latter being confirmed by scanning electron microscopy (Figure 4, P–R). The reduced and shortened cilia in both mutants support a role for Armc9 and Togaram1 in zebrafish cilium formation and/or stability.

JBTS-associated ARMC9 and TOGARAM1 variants result in decreased ciliary length. To gain insight into the ciliary defects associated with JBTS in humans, we evaluated 4 fibroblast lines from patients with *ARMC9*-associated JBTS. Western blot analysis of total protein lysates revealed that all 4 cell lines expressed trace levels of the 2 major ARMC9 isoforms at 92 kDa and 75.5 kDa seen

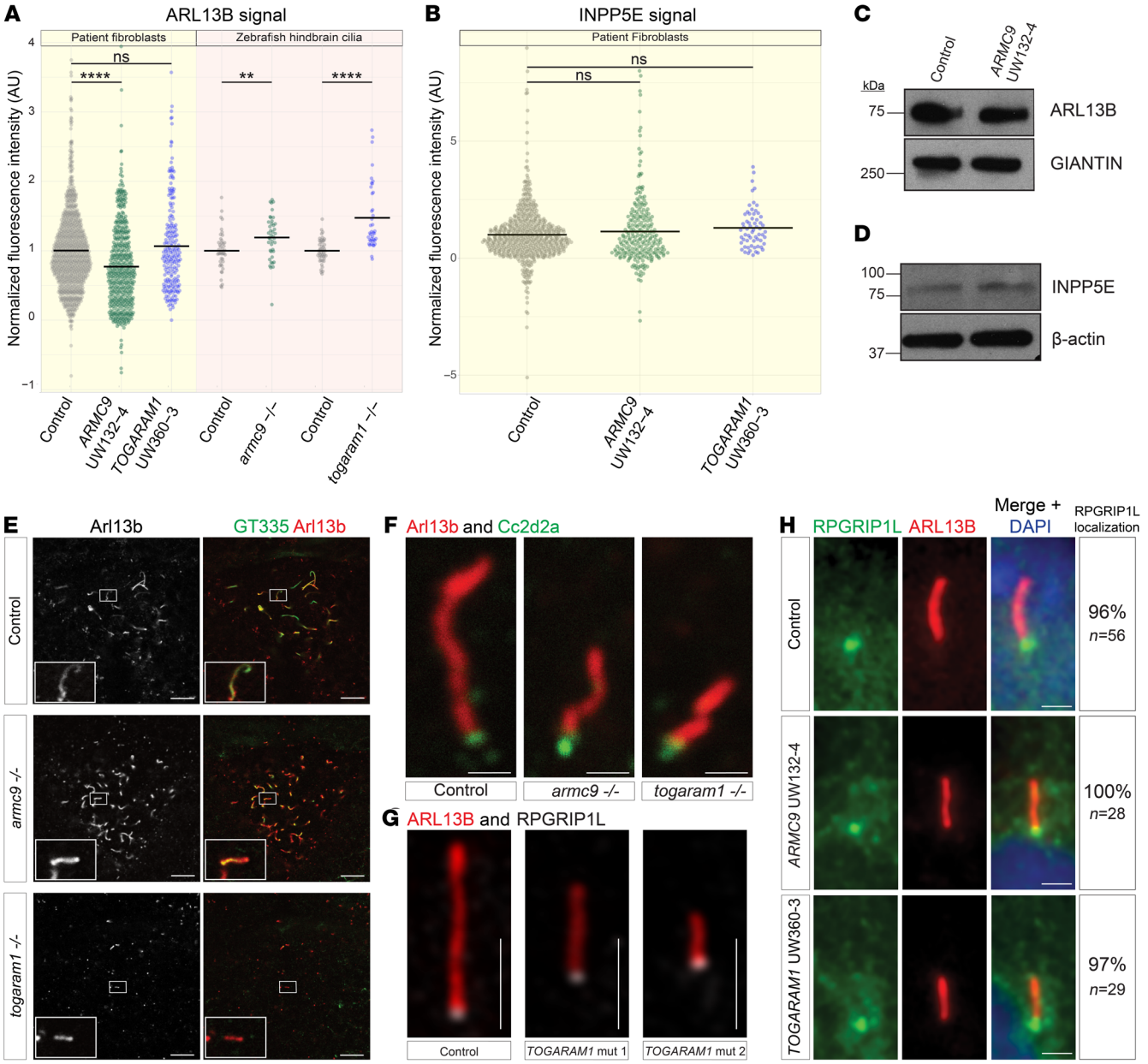

Figure 6. ARMC9 or TOGARAM1 dysfunction does not grossly affect the TZ. (**A**) Normalized relative fluorescence intensity of ARL13B signal in human fibroblast cilia (yellow panel; data were pooled from 3 experiments; control [gray] $n = 1089$, *ARMC9* [green] $n = 582$, and *TOGARAM1* [blue] $n = 126$) and in 3-dpf zebrafish hindbrain cilia (pink panel; data were pooled from 4 experiments; 10 cilia were measured per larva; each data point represents 1 larva; control *armc9* [gray] $n = 42$, *armc9*$^{-/-}$ [green] $n = 41$, control *togaram1* [gray] $n = 45$, *togaram1*$^{-/-}$ [blue] $n = 40$). Bars represent the mean. Controls were WT, +/+, or +/− siblings of −/−. Statistical significance was assessed using a Student's *t* test for both human fibroblast (Bonferroni-adjusted $P < 0.025$) and zebrafish ($P < 0.05$) experiments. $^{**}P \leq 0.01$ and $^{****}P \leq 0.0001$. (**B**) Normalized relative fluorescence intensity of INPP5E signal in human fibroblast cilia (data were pooled from 3 experiments: control [gray] $n = 620$, *ARMC9* [green] $n = 248$, *TOGARAM1* [blue] $n = 62$). See Supplemental Figure 7 for ARL13B and INPP5E signal intensity across all *ARMC9* fibroblast lines. Results were not significant using an unpaired Student's *t* test. (**C** and **D**) Western blot analysis of ARL13B (**C**) and INPP5E (**D**) in *ARMC9* UW132-4 patient fibroblasts. GIANTIN and β-actin served as loading controls, respectively. (**E**) Representative immunofluorescence signal for Arl13b (red) and polyglutamylated (green) in the 3-dpf zebrafish hindbrain cilia quantified in **A**. Scale bars: 10 μm. Original magnification, ×3.5 (insets). (**F**) Single hindbrain cilia stained with Arl13b (red) and Cc2d2a (green) in 3-dpf control, *armc9*$^{-/-}$, and *togaram1*$^{-/-}$ zebrafish. Scale bars: 1 μm. (**G**) Representative immunofluorescence signal for RPGRIP1L (white) and ARL13B (red) in cilia from control and 2 *TOGARAM1*-mutant hTERT-RPE1 lines. Scale bars: 2 μm. (**H**) Representative immunofluorescence for RPGRIP1L (green) and ARL13B (red) in *ARMC9* and *TOGARAM1* patient fibroblasts. Percentages of cilia with robust RPGRIP1L puncta are indicated. Scale bars: 2 μm.

in control fibroblasts (32) (Figure 5, A and B). To evaluate the ciliary phenotypes, we serum starved control and affected cells and then stained them with anti-acetylated α-tubulin and anti-ARL13B antibodies. All 4 patient cell lines displayed significantly shorter mean ciliary lengths (2.3–3.3 μm, standard deviation [SD] 0.7–1.4, $n = 349$–1395 cilia) compared with control cell ciliary lengths (3.6 μm, SD 1.4, $n = 1395$ cilia) (Figure 5C). Ciliation rates 48 hours after serum starvation were similar in the patient cell lines (75%–

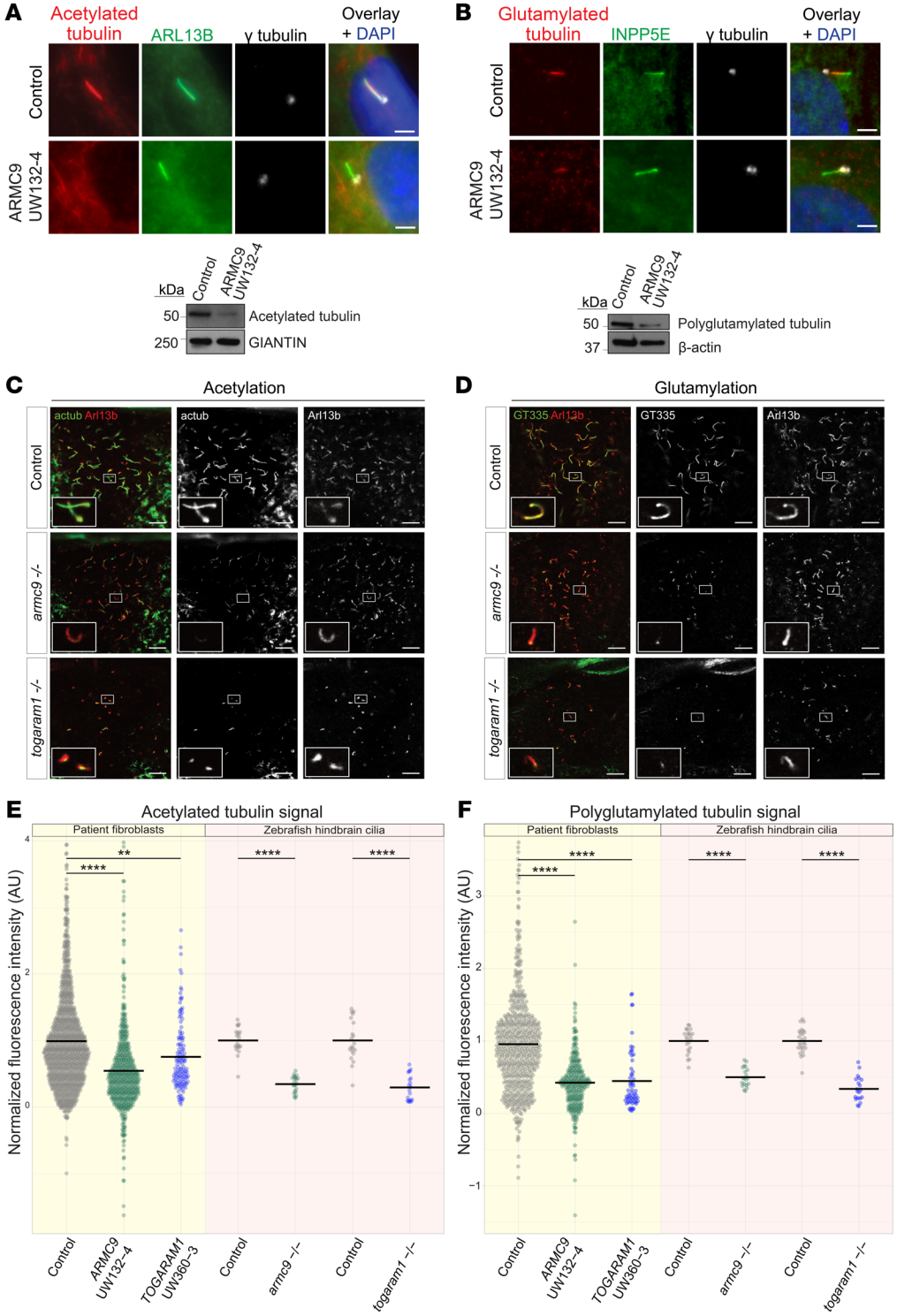

Figure 7. ARMC9- and TOGARAM1-mutant cilia display reduced tubulin PTMs in both patient fibroblasts and zebrafish ventricular cells. (**A** and **B**) Immunofluorescence images and immunoblots of (**A**) acetylated and (**B**) polyglutamylated tubulin in *ARMC9* patient fibroblasts versus control. In the immunoblots, GIANTIN and β-actin were used as loading controls. Scale bars: 3 μm. (**C** and **D**) Representative immunofluorescence images of 3-dpf zebrafish hindbrain cilia marked with Arl13b (red) and acetylated (green in **C**) or polyglutamylated (green in **D**) tubulin. Scale bars: 10 μm. Original magnification, ×3.5 (insets). Note that acetylated tubulin also marks axons in the developing brain, visible at the edges of the image in **C**. (**E**) Normalized relative fluorescence intensity for acetylated tubulin signal in human fibroblast cilia (yellow panel: control $n = 1106$, *ARMC9* $n = 532$, and *TOGARAM1* $n = 131$) and zebrafish hindbrain cilia (pink panel: pooled data from 2 experiments; 10 cilia measured per larva; each data point represents 1 larva; *armc9* control [gray] $n = 20$, *armc9*$^{-/-}$ [green] $n = 21$, *togaram1* control [gray] $n = 20$, *togaram1*$^{-/-}$ [blue] $n = 20$). (**F**) Normalized relative fluorescence intensity for polyglutamylated tubulin assessed in human fibroblast cilia (yellow panel: pooled from 3 experiments; control $n = 602$, *ARMC9* $n = 298$, and *TOGARAM1* $n = 58$) and zebrafish hindbrain cilia (pink panel: pooled data from 2 experiments; 10 cilia measured per larva; *armc9* control [gray] $n = 22$, *armc9*$^{-/-}$ [green] $n = 20$, *togaram1* control [gray] $n = 25$, *togaram1*$^{-/-}$ [blue] $n = 20$). Zebrafish controls were WT, +/+, or +/− siblings of −/−. In **E** and **F**, data points greater than 4 and less than or equal to 2 are not displayed but were included in the statistical analysis. For a complete graph of all data points and a graphical summary of all *ARMC9* lines, see Supplemental Figure 8, A and B and C and D, respectively. Statistical significance (adjusted $P < 0.025$) was assessed using a Bonferroni-corrected Student's *t* test for both fibroblast and zebrafish experiments. $^{**}P \le 0.01$ and $^{****}P \le 0.0001$.

86%) compared with control cells (80%), suggesting that ARMC9 does not play an integral role in ciliogenesis (Figure 5D).

Mean ciliary length was also shorter in the 1 available cell line from patient UW360-3 with *TOGARAM1*-related JBTS (2.6 μm, SD 0.8, $n = 154$ cilia) compared with the control (3.0 μm, SD 1.0, $n = 179$ cilia) (Figure 5E). This cell line had a slightly lower ciliation rate than did the control cells (85% versus 91%, respectively) (Figure 5F). To generate additional data on the effects of

loss of TOGARAM1 function on cilia in human cells, we turned to CRISPR/Cas9 genome-edited *TOGARAM1* hTERT-RPE1–mutant cells. Guide RNAs (gRNAs) targeting the translation start site of exon 1 resulted in 2 different cell lines harboring a disruption in the ATG site of both alleles of *TOGARAM1* (Supplemental Figure 5). These cell lines make significantly shorter cilia (mutant line 1: 1.5 μm, SD 0.6, n = 111 cilia; mutant line 2: 1.2 μm, SD 0.5, n = 178 cilia) compared with those of the isogenic control patient fibroblasts (2.3 μm, SD 0.8, n = 137 cilia) (Figure 5E). Ciliation levels in the *TOGARAM1* engineered cell lines (81% in mutant 1 and 69% in mutant 2) did not differ significantly from ciliation levels in the isogenic control fibroblasts (67%) (Figure 5F). Taken together, these results suggest that disruptions in *TOGARAM1* and *ARMC9* lead to shorter ciliary lengths but do not affect overall ciliation rates.

TZ integrity with ARMC9 and TOGARAM1 dysfunction. Given the well-described role of TZ dysfunction in JBTS (22), we evaluated whether the integrity of this compartment is affected by loss of TOGARAM1 or ARMC9 function. Since TZ dysfunction often results in loss of ciliary ARL13B, which secondarily causes loss of ciliary INPP5E (12, 49), we performed quantitative immunofluorescence (qIF) on control, *ARMC9*, and *TOGARAM1* patient cell lines. Our data revealed mildly lower levels of ARL13B in 3 of 4 *ARMC9* patient fibroblast lines and normal levels in the *TOGARAM1* patient fibroblast line (Figure 6A, and Supplemental Figure 8, A and C). Importantly, the mildly lower ARL13B levels observed in 3 of 4 ARMC9 cell lines were not associated with lower ciliary INPP5E (Figure 6B and Supplemental Figure 8B), indicating that the lower ARL13B levels were still sufficient to properly localize INPP5E. Western blot analysis also revealed similar levels of ARL13B and INPP5E in patient fibroblast lysates compared with levels in control cells (Figure 6, C and D). In zebrafish, Arl13b levels were not lower in either mutant (and were even slightly increased in the *armc9*$^{-/-}$ fish) (Figure 6, A, E, and F). Together, these results are strikingly different from the marked ciliary ARL13B and INPP5E reduction observed in TZ mutants (12, 49). To evaluate the composition of the TZ directly, we performed immunostaining for canonical TZ proteins RPGRIP1L in human cell lines (Figure 6, G and H) and Cc2d2a in zebrafish (Figure 6F). Both proteins localized normally to the TZ of the respective cilia. Taken together, these findings suggest that the TZ is generally intact, despite dysfunction of the ARMC9-TOGARAM1 complex.

TOGARAM1 dysfunction results in attenuated Smoothened translocation. Recent work has reported Hh signaling defects in cell lines with dysfunction of the JBTS genes *CEP104*, *CSPP1*, and *Armc9* (33, 39). Therefore, we tested whether *TOGARAM1* dysfunction leads to attenuated ciliary Smoothened (SMO) accumulation in response to Hh stimulation in the engineered *TOGARAM1*-mutant hTERT-RPE1 cells described above (Supplemental Figure 5). We starved the cells for 24 hours to promote ciliation and then exposed them to 100 nM SMO agonist (SAG) for an additional 24 hours before fixation and qIF (Supplemental Figure 9A). Upon pathway stimulation, the control and 2 *TOGARAM1*-mutant cell lines exhibited a significant induction of SMO translocation into the cilium as compared with DMSO-treated cells; however, the ciliary enrichment of SMO was markedly lower in the 2 mutant lines compared with control cells (Supplemental Figure 9, B–D). Overall, SMO intensity levels in both *TOGARAM1*-mutant lines were less than 50% of the control line, and the mutant cell lines did not differ significantly in their response when compared with each other.

ARMC9 and TOGARAM1 dysfunction affects tubulin PTMs in patient fibroblasts and zebrafish mutants. During our experiments evaluating ciliary ARL13B and INPP5E, we noted that the acetylated α-tubulin and polyglutamylated tubulin signals appeared substantially less intense in patient cell lines compared with control cells (Figure 7, A and B). Using qIF, we found that the mean acetylated tubulin levels were approximately 50% of control levels in the *ARMC9* lines and approximately 70% of control levels in the *TOGARAM1* line (Figure 7, E and F, and Supplemental Figure 10, A and B). Mean polyglutamylated signal levels were approximately 35% and approximately 45% of control levels in the *ARMC9* and *TOGARAM1* cell lines, respectively (Figure 7, B and F, and Supplemental Figure 10). Western blots of whole-cell lysates also demonstrated substantially lower levels of both acetylated and polyglutamylated tubulin in *ARMC9* fibroblast lines compared with levels in control fibroblasts (Figure 7, A and B). In the zebrafish *armc9*- and *togaram1*-mutant cell lines, we observed similar reductions of ciliary acetylated and polyglutamylated tubulin in the remaining ventricular cilia (Figure 7, C–F). Together, these results indicate that loss of either ARMC9 or TOGARAM1 results in decreased PTMs of axonemal tubulin across multiple model systems.

ARMC9 and TOGARAM1 dysfunction is associated with abnormal ciliary resorption. Posttranslational microtubule modifications such as acetylation and polyglutamylation are enriched in the ciliary compartment and play roles in ciliogenesis, axoneme stability, and cilium disassembly (17). To investigate the consequence of reduced ciliary microtubule PTMs on axonemal stability, we evaluated cilia of control and *ARMC9* patient cells for sensitivity to cold-induced microtubule depolymerization (50, 51). In control cells, a 10-minute treatment at 4°C was not associated with reduced numbers of cilia, while cold-treated *ARMC9* patient cells had 20%–30% fewer cilia than did untreated cells (Figure 8A). *TOGARAM1* patient cell cilia were also more susceptible to cold-induced depolymerization, with 15% fewer cilia after treatment compared with untreated cells (Figure 8A).

As a second measure of cilium stability, we evaluated the rate of cilium resorption after serum re-addition to serum-starved cells. Serum provides growth factors that quickly initiate ciliary resorption, so that cells can re-enter the cell cycle. In controls, the ciliation rate was approximately 85% of baseline 4 hours after serum re-addition. In contrast, the ciliation rate was 70% of baseline in *ARMC9* patient fibroblasts only 2 hours after serum re-addition, and by 8 hours, it was down to 50% compared with 75% in control cells (Figure 8B). To determine whether the faster resorption was due to an overactive deacetylating enzyme in the *ARMC9* cell lines, we repeated these experiments with and without the histone deacetylase 6 (HDAC6) inhibitor tubacin. Tubacin treatment did not rescue the faster resorption in *ARMC9* cell lines to control levels (Supplemental Figure 11, A–C). Intriguingly, the ciliation rate of the one *TOGARAM1* patient fibroblast line avail-

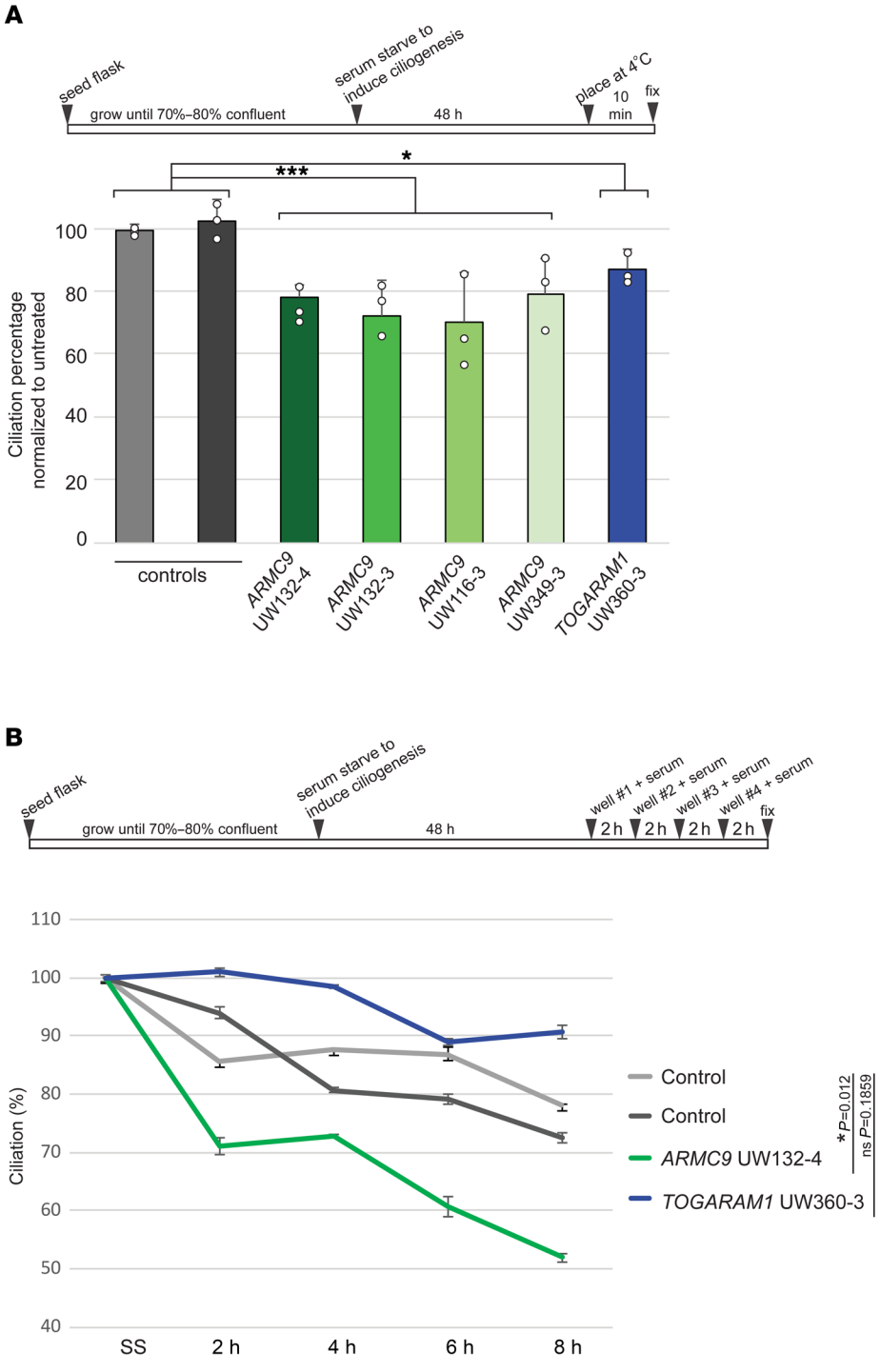

Figure 8. Fibroblasts from patients with JBTS exhibit abnormal axonemal stability. (**A**) Cold-induced depolymerization assay schematic and ciliation percentages of treated cells normalized to nontreated controls. Statistical significance was assessed using a Bonferroni-corrected Kruskal-Wallis test, with $P = 0.0003$ and $P = 0.02$, respectively. White circles represent individual experiments. (**B**) Relative ciliation rates 2, 4, 6, and 8 hours after serum re-addition in human fibroblasts previously serum starved for 48 hours. At *t*0, *t*2, *t*4, *t*6, and *t*8 hours, respectively, the following numbers of cells were quantified: control 1, $n = 455$, $n = 413$, $n = 350$, $n = 346$, $n = 395$; control 2, $n = 595$, $n = 431$, $n = 351$, $n = 368$, $n = 279$; *ARMC9* UW132-4, $n = 218$, $n = 193$, $n = 229$, $n = 195$, $n = 189$; and *TOGARAM1* UW360-3, $n = 496$, $n = 622$, $n = 513$, $n = 558$, $n = 492$. Ciliation percentages were normalized to 100% at the time of serum re-addition, and percentages represent the amount of remaining cilia compared with *t*0. Error bars represent 95% CIs. See the "Statistics and reproducibility" section of Supplemental Methods for details on statistical testing for cilia stability assays.

able remained 90% of baseline even 8 hours after serum re-addition, which was substantially higher than the ciliation rate in control fibroblasts (Figure 8B). To determine whether this abnormal ciliary stability caused defects in cell-cycle progression, we used a flow cytometry–based approach to quantify cell-cycle re-entry (Supplemental Figure 12, A and B). *ARMC9* and *TOGARAM1* patient cell lines re-entered the cell cycle closely, with timing similar to that of control cells. These data suggest that the ARMC9-TOGARAM1 complex plays a role in regulating axonemal stability.

Discussion

In this study, we identified a JBTS-associated protein module that can be distinguished physically and functionally from the previously described JBTS protein complex at the ciliary TZ of primary cilia (52). Several components of this new module localize at the ciliary basal body (32) and at the proximal end of the ciliary axoneme (33, 53). Pathogenic variants in the genes encoding 2 directly interacting members of the module, ARMC9 and TOGARAM1, cause defects in cilium length, Hh signaling (SMO translocation), microtubule PTMs (acetylation and polyglutamylation), and ciliary stability in patient-derived fibroblasts, zebrafish mutants, and genetically edited hTERT-RPE1 cell lines (summary shown in Figure 9).

The ARMC9-TOGARAM1 complex in JBTS. Knowledge of the components and associations of the ciliary molecular machinery has been instrumental for relating ciliopathy genetic defects, associated pathomechanisms, and the wide spectrum of overlapping ciliopathy phenotypes. Several affinity and proximity proteomics approaches have been used to determine the topology of ciliary protein-protein interaction networks and to generate molecular blueprints of the ciliary machinery, e.g., the entire ciliary organelle (54), of the human centrosome-cilium interface (53), or specific ciliopathy-associated protein modules (55, 56). The majority of the previously identified JBTS-associated proteins partic-

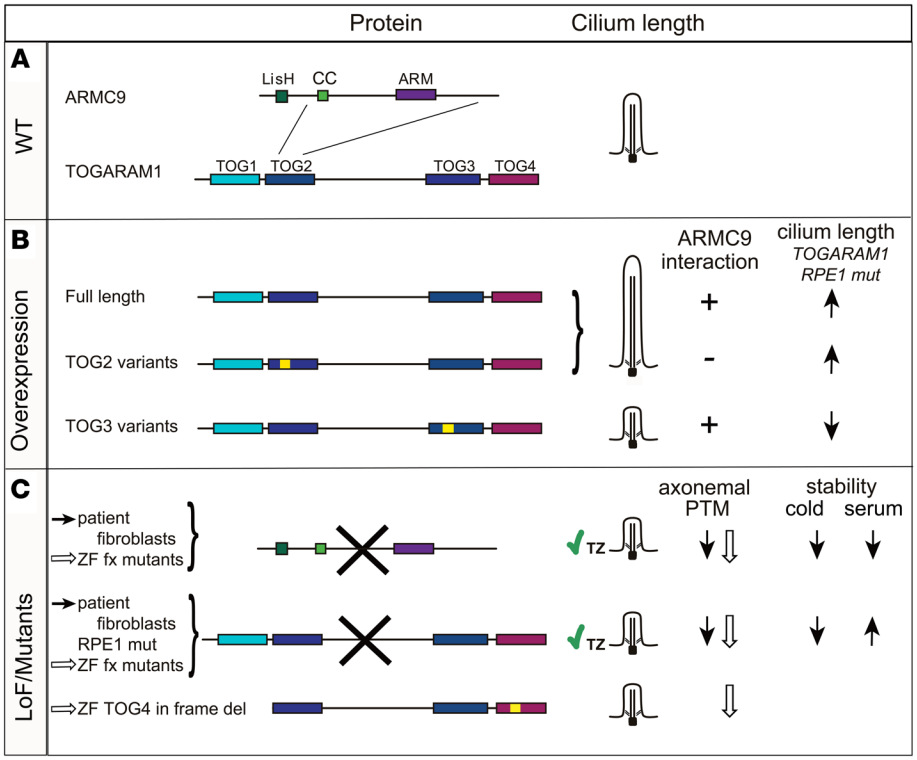

Figure 9. Disruptions of the ARMC9-TOGARAM1 module affect ciliary length, axonemal PTMs, and stability. (**A**) TOGARAM1 interacts with ARMC9 through its TOG2 domain. (**B**) Effects of TOGARAM1 overexpression (WT and with JBTS-associated variants) on ciliary length in *TOGARAM1*-mutant hTERT-RPE1 cells and consequences of JBTS-associated variants for the interaction with ARMC9. (**C**) Consequences of mutations in *ARMC9* or *TOGARAM1* for ciliary length and axonemal PTMs in patient fibroblast lines (black arrows) or zebrafish mutants (white arrows). TZ integrity despite *ARMC9* or *TOGARAM1* dysfunction is indicated with a green checkmark. The consequences of *TOGARAM1* and *ARMC9* mutations for ciliary stability in response to cold or serum re-addition in patient fibroblasts are indicated with black arrows. Yellow boxes represent pathogenic variants. Bold crosses indicate presumed loss-of-function mutations. del, deletion; fx, frameshift; LoF, loss of function; ZF, zebrafish; RPE1 mut, hTERT-RPE1 TOGARAM1–mutant lines. Protein domains: LisH, CC, ARM, TOG.

ipate in specific submodules of complex ciliary protein networks that vary in subciliary localization, concentrating at the TZ to organize and regulate the ciliary gate (12, 57).

Using a combination of affinity proteomics (TAP) and Y2H protein interaction screens, we found that the newly JBTS-associated protein ARMC9 interacted with known JBTS-associated proteins CSPP1 and CEP290, confirming the importance of this complex to JBTS. We also identified 2 ciliary microtubule–associated proteins, TOGARAM1 and CCDC66, that were not previously associated with JBTS. A subsequent TAP screen using TOGARAM1 as bait pulled out ARMC9, further validating their interaction, and also identified another JBTS-associated protein, CEP104 (JBTS25). With Y2H screening we determined the direct interaction of TOGARAM1 with another JBTS-associated protein, RPGRIP1L (JBTS7), whereas a TAP experiment using CSPP1 as a bait again identified CEP290 as a complex member and confirmed its previously identified interaction with RPGRIP1L (58). Our results are in agreement with the BioID proximity interactome of CEP104 that contained most of our module components, except for ARMC9 and RPGRIP1L (53). Co-IP and Y2H analyses validated the core module, ARMC9, TOGARAM1, CCDC66, and CEP104, consisting of proteins important for cilium function and ciliopathy disease. For instance, CCDC66 was previously found to interact with CEP290 (36), and null mutations cause retinal degeneration in dogs (59) and mice (60). CEP104 localizes to both the daughter centriole as well as to the apical tip of a growing cilium (30) and, like TOGARAM1, interacts with tubulin through its TOG domain (61). Moreover, CEP104 has been shown to interact with NEK1 (61), which is associated with the ciliopathy "short-rib polydactyly syndrome Majewski type" (62) and with the JBTS-associated protein CSPP1 (39). This interaction, which we confirmed in our co-IP experiments, is required for the formation of Hh signaling–competent cilia, as mutations in CSPP1 and CEP104 significantly decreased ciliary SMO translocation (39), similar to what we observed with RPE1 *TOGARAM1*-mutant lines. Following the "guilt-by-association" paradigm, we next found biallelic *TOGARAM1* variants in multiple individuals with JBTS, reiterating the relevance of the complex to JBTS and moving us closer to identifying all genetic causes of this disorder. We did not find *CCDC66* variants in any of the more than 600 families affected by JBTS, indicating that variants in this gene are, at most, a very rare cause of JBTS.

Role of the ARMC9-TOGARAM1 complex in ciliary length and stability. The structure of TOG domains is highly conserved for microtubule binding, where the intra-HEAT loop in the discontinuous TOG domain binds tubulin (63–66). TOG domains are thought to regulate microtubule growth and dynamics (67). The TOG domains in TOGARAM1 have differential microtubule binding capacity and likely function in concert to coordinate microtubule polymerization (34). For example, the C-terminal TOG domains TOG3 and TOG4 promote microtubule lattice binding (34). Interestingly, we found that cilia were shorter in cells with *ARMC9* or *TOGARAM1* dysfunction. In contrast, we demonstrate that TOGARAM1 overexpression resulted in long cilia and that this effect required an intact TOG3 domain, but not an intact TOG2 domain, which was required for TOGARAM1 interaction with ARMC9. In fact, the TOG3 domain Arg1311Cys variant did not interfere with the ARMC9 interaction, but overexpression of this mutant protein resulted in severely shortened cilia. Since both long and short cilia have been identified in fibroblasts from patients with different genetic causes of JBTS, no simple correlation between cilium length and JBTS disease mechanism can be made (31, 32, 68, 69).

Recent work in *Tetrahymena* indicates that *TOGARAM1* and *ARMC9* orthologs may have opposite effects on B-tubule length (29). In mammalian cells, we found that dysfunction of either gene led to shorter cilia, decreased PTMs, and sensitivity to cold-induced ciliary microtubule depolymerization, indicating reduced ciliary stability. Intriguingly, TOGARAM1 and ARMC9 dysfunction seemed to have opposite effects on the kinetics of cilium resorption after serum re-addition in patient fibroblasts. This result suggests that different mechanisms may underlie ciliary resorption in the setting of serum re-addition versus cold-induced depolymerization. The latter may represent an acute stressor directly correlated with cilium stability, whereas the former is a regulated mechanism required for cell-cycle re-entry, for which TOGARAM1 and ARMC9 may indeed play opposing roles, as suggested by the work in *Tetrahymena* (29).

PTMs of ciliary microtubules. *ARMC9* and *TOGARAM1* dysfunction also led to significantly decreased axonemal PTMs (polyglutamylation and acetylation) in patient fibroblasts and zebrafish, supporting the relevance of altered PTMs in JBTS. Tubulin PTMs are indispensable for proper microtubule function, affecting their mechanical properties, stability, and binding of microtubule-associated proteins (MAPs) to influence protein trafficking and signaling (17).

Polyglutamylation decorates the surface of axonemal microtubules. This reversible modification ranges from 1–17 glutamyl residues in vivo (70) and plays a role in intraflagellar transport activity and MAP binding (71–74). Decreased ciliary polyglutamylation interferes with kinesin 2–mediated anterograde transport, also on the B-tubule, and subsequently negatively impacts Hh signaling (72, 73). Some MAPs are sensitive to the amount of glutamylation. For example, spastin has optimal microtubule-severing activity in vitro with moderate polyglutamylation, whereas both hypo- and hyperglutamylation suppress severing activity (75). In the context of JBTS, decreased axonemal polyglutamylation was reported in fibroblasts from patients with *CEP41*-related JBTS (11). More recent work found decreased axonemal glutamylation with *ARL13B*, *FIP5*, and *TTLL5* knockdown in immortalized cells, which was associated with effects on polycystin localization and Hh signaling (71).

While most PTMs are added to the C-terminus of tubulin on the microtubular surface, acetylation uniquely occurs on the luminal surface of α-tubulin. Ciliary resorption requires removal of this modification by HDAC6 (76). It has long been observed that the hyperstabilized ciliary microtubules are acetylated, but until recently it was not known if the modification confers stability or if long-lived stable microtubules accumulate this modification. Recent work using cryogenic electron microscopy (cryo-EM) confirmed that acetylation causes a stabilizing conformational change (77). This is in line with our findings of decreased axonemal microtubule acetylation and stability with ARMC9 and TOGARAM1 dysfunction, as well as with previously published findings of *Kif7* and *Armc9* dysfunction (33, 68). In particular, *Armc9*-null NIH3T3 cells had short cilia and decreased acetylation and glutamylation. The more rapid ciliary resorption with ARMC9 dysfunction was unlikely to be due to excessive deacetylation, since cilia were not stabilized by HDAC6 inhibition. Interestingly, *Kif7*-mutant mouse embryonic fibroblasts (MEFs) exhibited reduced glutamylation, making it the only other JBTS model with decreases in both of these PTMs (31, 68). Fibroblasts from patients with *INPP5E*-related JBTS also display decreased cilium stability (78). Notably, these models of *KIF7*- and *INPP5E*-related ciliary dysfunction disrupt Hh signaling, probably because of GLI/SUFU mislocalization and aberrant phosphatidylinositol composition, respectively, while emerging evidence indicates that reduced polyglutamlyation may indirectly alter translocation of Hh pathway components by perturbing anterograde intraflagellar transport (71, 72).

The observed reduction of PTMs with *ARMC9* and *TOGARAM1* dysfunction could therefore affect ciliary function through loss of stability and/or direct disruption of signaling pathways. In fact, *Armc9* and *Togaram1* (FAM179B) were identified as positive regulators of the Hh pathway in a genome-wide screen for Hh signaling components (33). That study also demonstrated that overexpressed ARMC9 translocates from the ciliary base to the tip upon Hh pathway stimulation (33). In *Tetrahymena*, orthologs of ARMC9 and TOGARAM1 are seen at both the base and tip, with tip enrichment during cilia regeneration (29). Taken together, these results suggest a dynamic localization of the complex members and likely changes in protein complex composition at each locale. Further work will be required to determine the details of dynamic ARMC9-TOGARAM1 localization during ciliogenesis, resorption, and signaling.

Conclusions. The biological mechanisms underlying JBTS remain incompletely understood. We believe this work brings us one step closer to the complete catalog of JBTS genetic causes and highlights the role of a new JBTS-associated protein complex including ARMC9 and TOGARAM1. Approximately half of JBTS-associated genes are implicated in TZ function, which is required for ciliary ARL13B and INPP5E localization. In contrast, the ARMC9-TOGARAM1 complex is not required for INPP5E localization and, instead, appears to regulate the PTM of ciliary microtubules, ciliary length, and ciliary stability. Future work will need to reconcile how the diverse array of cellular defects associated with loss of function for the JBTS genes relate to this important human disorder.

Methods

A detailed description of cell culturing conditions, cloning, immunofluorescence and microscopy, cell-cycle assay, zebrafish experiments, PalmMyr assay, TAP, Y2H interaction analysis, co-IP, statistical analysis, microtubule cold assay, cilia stability assay, subject ascertainment and phenotypic data, variant identification, and array comparative genomic hybridization (CGH) can be found in the Supplemental Methods. Full, uncropped and unedited images of all gels and Western blots are included in the supplemental material.

Additional web resources

CHOPCHOP was used to design guide RNAs for zebrafish genome editing of togaram1 (http://chopchop.cbu.uib.no). Data from Ensembl (https://www.ensembl.org/index.html) were used to generate the transcript schematic shown in Figure 2C. PlotsOfData (https://huygens.science.uva.nl/PlotsOfData/) (79) was used to visualize the data and generate all dot plots. Phylogeny (http://www.phylogeny.fr/) was

used for phylogenetic analysis in Supplemental Figure 6A. Synteny (http://syntenydb.uoregon.edu/synteny_db/) was used for analysis in Supplemental Figure 6, B and C.

Author contributions

RBG, RR, and DD conceived the overall project. BLL, JCVDW, TDSR, JCD, SCFN, KB, MU, MK, JAS, FSA, RBG, RR, DD, DAN, and MJB designed experiments and led the data generation and processing. BLL, JCVDW, TDSR, SJFL, AG, AK, MA, MEG, SECVB, CVM, MG, and UWCMG performed experiments. RS, MC, HM, and JCD acquired clinical phenotype data. BLL, JCVDW, TDSR, MBG, MEG, CVM, RBG, RR, and DD analyzed and interpreted data. BLL, JCVDW, TDSR, RBG, RR, and DD wrote the manuscript with input from all authors. The order of the coauthors was decided based on the focus on the protein interaction aspect of the work and the author order in related publications.

Acknowledgments

We thank the patients and parents for their participation in this research. We thank David Breslow (Yale University) and Max Nachury (UCSF) for providing the ARMC9-3xFlag IMCD3 FlpIn lines and NIH 3T3 ARMC9 mutant lines. The research leading to these results has received funding from the Netherlands Organisation for Scientific Research (NWO Vici-865.12.005, to RR); the Netherlands Organisation for Health Research and Development (ZonMW, 91216051, to RR); the Foundation Fighting Blindness (PPA-0717-0719-RAD, to MU and RR); the Tistou & Charlotte Kerstan Stiftung (to MU); the Swiss National Science Foundation (SNF) (PP00P3_170681, to RBG and 31003A_173083, to SCFN); the Zurich Neuroscience Center (to RBG); the NIH Eunice Kennedy Shriver National Institute of Child Health and Human Development (U54HD083091 Genetics Core and sub-project 6849, to DD and F32 HD095599, to JVDW); private donations (to DD); the Watson Genetic Laboratory (Tehran, Iran) for WGL-1914 sequencing (to MK); the National Human Genome Research Institute, NIH (U54HG006493, to MB and DN); Kidney Research UK; the Northern Counties Kidney Research Fund (joint studentship ST_001_20171120, to MBG and 18/01, to JAS); and the King Salman Center for Disability Research (to FSA). Part of the data presented here were provided through access to the data and findings generated by the 100,000 Genomes Project, which is funded by the National Institute for Health Research (NIHR) and National Health Service (NHS) England.

Address correspondence to: Ruxandra Bachmann-Gagescu, University of Zurich, Institute of Medical Genetics, Wagistrasse 12, 8952 Schlieren, Switzerland. Email: ruxandra.bachmann@imls.uzh.ch. Or to: Ronald Roepman, Department of Human Genetics (855), Radboud University Medical Center, P.O. Box 9101, 6500 HB Nijmegen, Netherlands. Email: ronald.roepman@radboudumc.nl. Or to: Dan Doherty, Department of Pediatrics, University of Washington, Box 356320, 1959 N.E. Pacific St., RR-247, Seattle, WA 98195, USA. Email: ddoher@uw.edu.

1. Hildebrandt F, Benzing T, Katsanis N. Ciliopathies. *N Engl J Med*. 2011;364(16):1533–1543.
2. van Reeuwijk J, Arts HH, Roepman R. Scrutinizing ciliopathies by unraveling ciliary interaction networks. *Hum Mol Genet*. 2011;20(R2):R149–R157.
3. Satir P, Pedersen LB, Christensen ST. The primary cilium at a glance. *J Cell Sci*. 2010;123(Pt 4):499–503.
4. Maria BL, et al. "Joubert syndrome" revisited: key ocular motor signs with magnetic resonance imaging correlation. *J Child Neurol*. 1997;12(7):423–430.
5. Sattar S, Gleeson JG. The ciliopathies in neuronal development: a clinical approach to investigation of Joubert syndrome and Joubert syndrome-related disorders. *Dev Med Child Neurol*. 2011;53(9):793–798.
6. Reiter JF, Leroux MR. Genes and molecular pathways underpinning ciliopathies. *Nat Rev Mol Cell Biol*. 2017;18(9):533–547.
7. Shamseldin HE, et al. The morbid genome of ciliopathies: an update. *Genet Med*. 2020;22(6):1051–1060.
8. Bachmann-Gagescu R, et al. Healthcare recommendations for Joubert syndrome. *Am J Med Genet A*. 2020;182(1):229–249.
9. Chaki M, et al. Exome capture reveals ZNF423 and CEP164 mutations, linking renal ciliopathies to DNA damage response signaling. *Cell*. 2012;150(3):533–548.
10. Bielas SL, et al. Mutations in INPP5E, encoding inositol polyphosphate-5-phosphatase E, link phosphatidyl inositol signaling to the ciliopathies. *Nat Genet*. 2009;41(9):1032–1036.
11. Lee JE, et al. CEP41 is mutated in Joubert syndrome and is required for tubulin glutamylation at the cilium. *Nat Genet*. 2012;44(2):193–199.
12. Garcia-Gonzalo FR, et al. A transition zone complex regulates mammalian ciliogenesis and ciliary membrane composition. *Nat Genet*. 2011;43(8):776–784.
13. Valente EM, et al. Mutations in TMEM216 perturb ciliogenesis and cause Joubert, Meckel and related syndromes. *Nat Genet*. 2010;42(7):619–625.
14. Garcia-Gonzalo FR, et al. Phosphoinositides regulate ciliary protein trafficking to modulate hedgehog signaling. *Dev Cell*. 2015;34(4):400–409.
15. Piperno G, Fuller MT. Monoclonal antibodies specific for an acetylated form of alpha-tubulin recognize the antigen in cilia and flagella from a variety of organisms. *J Cell Biol*. 1985;101(6):2085–2094.
16. Bré MH, de Néchaud B, Wolff A, Fleury A. Glutamylated tubulin probed in ciliates with the monoclonal antibody GT335. *Cell Motil Cytoskeleton*. 1994;27(4):337–349.
17. Wloga D, Joachimiak E, Louka P, Gaertig J. Post-translational modifications of tubulin and cilia. *Cold Spring Harb Perspect Biol*. 2017;9(6):a028159.
18. Arts HH, et al. Mutations in the gene encoding the basal body protein RPGRIP1L, a nephrocystin-4 interactor, cause Joubert syndrome. *Nat Genet*. 2007;39(7):882–888.
19. Delous M, et al. The ciliary gene RPGRIP1L is mutated in cerebello-oculo-renal syndrome (Joubert syndrome type B) and Meckel syndrome. *Nat Genet*. 2007;39(7):875–881.
20. Gorden NT, et al. CC2D2A is mutated in Joubert syndrome and interacts with the ciliopathy-associated basal body protein CEP290. *Am J Hum Genet*. 2008;83(5):559–571.
21. Williams CL, et al. MKS and NPHP modules cooperate to establish basal body/transition zone membrane associations and ciliary gate function during ciliogenesis. *J Cell Biol*. 2011;192(6):1023–1041.
22. Shi X, et al. Super-resolution microscopy reveals that disruption of ciliary transition-zone architecture causes Joubert syndrome. *Nat Cell Biol*. 2017;19(10):1178–1188.
23. Cantagrel V, et al. Mutations in the cilia gene ARL13B lead to the classical form of Joubert syndrome. *Am J Hum Genet*. 2008;83(2):170–179.
24. Chávez M, Ena S, Van Sande J, de Kerchove d'Exaerde A, Schurmans S, Schiffmann SN. Modulation of ciliary phosphoinositide content regulates trafficking and sonic hedgehog signaling output. *Dev Cell*. 2015;34(3):338–350.
25. Caspary T, Larkins CE, Anderson KV. The graded response to sonic hedgehog depends on cilia architecture. *Dev Cell*. 2007;12(5):767–778.
26. Tuz K, et al. Mutations in CSPP1 cause primary cilia abnormalities and Joubert syndrome with or without Jeune asphyxiating thoracic dystrophy. *Am J Hum Genet*. 2014;94(1):62–72.
27. Shaheen R, et al. Mutations in CSPP1, encoding a core centrosomal protein, cause a range of ciliopathy phenotypes in humans. *Am J Hum Genet*. 2014;94(1):73–79.
28. Srour M, et al. Joubert Syndrome in French Canadians and Identification of Mutations in CEP104. *Am J Hum Genet*. 2015;97(5):744–753.
29. Louka P, et al. Proteins that control the geometry of microtubules at the ends of cilia. *J Cell Biol*. 2018;217(12):4298–4313.
30. Satish Tammana TV, Tammana D, Diener DR,

Rosenbaum J. Centrosomal protein CEP104 (Chlamydomonas FAP256) moves to the ciliary tip during ciliary assembly. *J Cell Sci*. 2013;126(Pt 21):5018–5029.
31. Dafinger C, et al. Mutations in KIF7 link Joubert syndrome with sonic hedgehog signaling and microtubule dynamics. *J Clin Invest*. 2011;121(7):2662–2667.
32. Van De Weghe JC, et al. Mutations in ARMC9, which encodes a basal body protein, cause Joubert syndrome in humans and ciliopathy phenotypes in zebrafish. *Am J Hum Genet*. 2017;101(1):23–36.
33. Breslow DK, et al. A CRISPR-based screen for hedgehog signaling provides insights into ciliary function and ciliopathies. *Nat Genet*. 2018;50(3):460–471.
34. Das A, Dickinson DJ, Wood CC, Goldstein B, Slep KC. Crescerin uses a TOG domain array to regulate microtubules in the primary cilium. *Mol Biol Cell*. 2015;26(23):4248–4264.
35. Jiang K, et al. A Proteome-wide screen for mammalian SxIP motif-containing microtubule plus-end tracking proteins. *Curr Biol*. 2012;22(19):1800–1807.
36. Conkar D, Culfa E, Odabasi E, Rauniyar N, Yates JR, Firat-Karalar EN. The centriolar satellite protein CCDC66 interacts with CEP290 and functions in cilium formation and trafficking. *J Cell Sci*. 2017;130(8):1450–1462.
37. Letteboer SJ, Roepman R. Versatile screening for binary protein-protein interactions by yeast two-hybrid mating. *Methods Mol Biol*. 2008;484:145–159.
38. Conkar D, Bayraktar H, Firat-Karalar EN. Centrosomal and ciliary targeting of CCDC66 requires cooperative action of centriolar satellites, microtubules and molecular motors. *Sci Rep*. 2019;9(1):14250.
39. Frikstad KM, et al. A CEP104-CSPP1 complex is required for formation of primary cilia competent in hedgehog signaling. *Cell Rep*. 2019;28(7):1907–1922.e6.
40. Zacharias DA, Violin JD, Newton AC, Tsien RY. Partitioning of lipid-modified monomeric GFPs into membrane microdomains of live cells. *Science*. 2002;296(5569):913–916.
41. Bachmann-Gagescu R, et al. Joubert syndrome: a model for untangling recessive disorders with extreme genetic heterogeneity. *J Med Genet*. 2015;52(8):514–522.
42. Karczewski KJ, et al. The mutational constraint spectrum quantified from variation in 141,456 humans. *Nature*. 2020;581(7809):434–443.
43. Rentzsch P, Witten D, Cooper GM, Shendure J, Kircher M. CADD: predicting the deleteriousness of variants throughout the human genome. *Nucleic Acids Res*. 2019;47(D1):D886–D894.
44. O'Roak BJ, et al. Exome sequencing in sporadic autism spectrum disorders identifies severe de novo mutations. *Nat Genet*. 2011;43(6):585–589.
45. Venselaar H, Te Beek TA, Kuipers RK, Hekkelman ML, Vriend G. Protein structure analysis of mutations causing inheritable diseases. An e-Science approach with life scientist friendly interfaces. *BMC Bioinformatics*. 2010;11:548.
46. Nithianantham S, Cook BD, Beans M, Guo F, Chang F, Al-Bassam J. Structural basis of tubulin recruitment and assembly by microtubule polymerases with tumor overexpressed gene (TOG) domain arrays. *Elife*. 2018;7:e38922.
47. Grimes DT, Boswell CW, Morante NF, Henkelman RM, Burdine RD, Ciruna B. Zebrafish models of idiopathic scoliosis link cerebrospinal fluid flow defects to spine curvature. *Science*. 2016;352(6291):1341–1344.
48. Bachmann-Gagescu R, et al. The ciliopathy gene cc2d2a controls zebrafish photoreceptor outer segment development through a role in Rab8-dependent vesicle trafficking. *Hum Mol Genet*. 2011;20(20):4041–4055.
49. Slaats GG, et al. MKS1 regulates ciliary INPP5E levels in Joubert syndrome. *J Med Genet*. 2016;53(1):62–72.
50. Piperno G, LeDizet M, Chang XJ. Microtubules containing acetylated alpha-tubulin in mammalian cells in culture. *J Cell Biol*. 1987;104(2):289–302.
51. LeDizet M, Piperno G. Cytoplasmic microtubules containing acetylated alpha-tubulin in Chlamydomonas reinhardtii: spatial arrangement and properties. *J Cell Biol*. 1986;103(1):13–22.
52. Reiter JF, Blacque OE, Leroux MR. The base of the cilium: roles for transition fibres and the transition zone in ciliary formation, maintenance and compartmentalization. *EMBO Rep*. 2012;13(7):608–618.
53. Gupta GD, et al. A dynamic protein interaction landscape of the human centrosome-cilium interface. *Cell*. 2015;163(6):1484–1499.
54. Boldt K, et al. An organelle-specific protein landscape identifies novel diseases and molecular mechanisms. *Nat Commun*. 2016;7:11491.
55. Toriyama M, et al. The ciliopathy-associated CPLANE proteins direct basal body recruitment of intraflagellar transport machinery. *Nat Genet*. 2016;48(6):648–656.
56. Sang L, et al. Mapping the NPHP-JBTS-MKS protein network reveals ciliopathy disease genes and pathways. *Cell*. 2011;145(4):513–528.
57. Garcia-Gonzalo FR, Reiter JF. Scoring a backstage pass: mechanisms of ciliogenesis and ciliary access. *J Cell Biol*. 2012;197(6):697–709.
58. Patzke S, et al. CSPP is a ciliary protein interacting with nephrocystin 8 and required for cilia formation. *Mol Biol Cell*. 2010;21(15):2555–2567.
59. Dekomien G, et al. Progressive retinal atrophy in Schapendoes dogs: mutation of the newly identified CCDC66 gene. *Neurogenetics*. 2010;11(2):163–174.
60. Gerding WM, et al. Ccdc66 null mutation causes retinal degeneration and dysfunction. *Hum Mol Genet*. 2011;20(18):3620–3631.
61. Al-Jassar C, et al. The ciliopathy-associated Cep104 protein interacts with tubulin and Nek1 kinase. *Structure*. 2017;25(1):146–156.
62. Thiel C, et al. NEK1 mutations cause short-rib polydactyly syndrome type majewski. *Am J Hum Genet*. 2011;88(1):106–114.
63. Howard AE, Fox JC, Slep KC. Drosophila melanogaster mini spindles TOG3 utilizes unique structural elements to promote domain stability and maintain a TOG1- and TOG2-like tubulin-binding surface. *J Biol Chem*. 2015;290(16):10149–10162.
64. Leano JB, Rogers SL, Slep KC. A cryptic TOG domain with a distinct architecture underlies CLASP-dependent bipolar spindle formation. *Structure*. 2013;21(6):939–950.
65. Slep KC. A cytoskeletal symphony: owed to TOG. *Dev Cell*. 2018;46(1):5–7.
66. Al-Bassam J, Kim H, Brouhard G, van Oijen A, Harrison SC, Chang F. CLASP promotes microtubule rescue by recruiting tubulin dimers to the microtubule. *Dev Cell*. 2010;19(2):245–258.
67. Leano JB, Slep KC. Structures of TOG1 and TOG2 from the human microtubule dynamics regulator CLASP1. *PLoS One*. 2019;14(7):e0219823.
68. He M, et al. The kinesin-4 protein Kif7 regulates mammalian hedgehog signalling by organizing the cilium tip compartment. *Nat Cell Biol*. 2014;16(7):663–672.
69. Srivastava S, et al. A human patient-derived cellular model of Joubert syndrome reveals ciliary defects which can be rescued with targeted therapies. *Hum Mol Genet*. 2017;26(23):4657–4667.
70. Geimer S, Teltenkötter A, Plessmann U, Weber K, Lechtreck KF. Purification and characterization of basal apparatuses from a flagellate green alga. *Cell Motil Cytoskeleton*. 1997;37(1):72–85.
71. He K, et al. Axoneme polyglutamylation regulated by Joubert syndrome protein ARL13B controls ciliary targeting of signaling molecules. *Nat Commun*. 2018;9(1):3310.
72. Hong SR, et al. Spatiotemporal manipulation of ciliary glutamylation reveals its roles in intraciliary trafficking and hedgehog signaling. *Nat Commun*. 2018;9(1):1732.
73. O'Hagan R, et al. Glutamylation regulates transport, specializes function, and sculpts the structure of cilia. *Curr Biol*. 2017;27(22):3430–3441.e6.
74. Orbach R, Howard J. The dynamic and structural properties of axonemal tubulins support the high length stability of cilia. *Nat Commun*. 2019;10(1):1838.
75. Valenstein ML, Roll-Mecak A. Graded control of microtubule severing by tubulin glutamylation. *Cell*. 2016;164(5):911–921.
76. Pugacheva EN, Jablonski SA, Hartman TR, Henske EP, Golemis EA. HEF1-dependent Aurora A activation induces disassembly of the primary cilium. *Cell*. 2007;129(7):1351–1363.
77. Eshun-Wilson L, et al. Effects of α-tubulin acetylation on microtubule structure and stability. *Proc Natl Acad Sci USA*. 2019;116(21):10366–10371.
78. Hardee I, et al. Defective ciliogenesis in INPP5E-related Joubert syndrome. *Am J Med Genet A*. 2017;173(12):3231–3237.
79. Postma M, Goedhart J. PlotsOfData – a web app for visualizing data together with their summaries. *PLoS Biol*. 2019;17(3):e3000202.